Fault and fluid interaction during the 2012 Emilia (Northern Italy) seismic sequence

Fonzetti R. [1, 2*], Valoroso L. [1], De Gori P. [1], Chiarabba C. [1]

1, Istituto Nazionale di Geofisica e Vulcanologia, Italy, Rome (RM)

2, Università degli Studi Roma Tre, Italy, Rome (RM)

**corresponding author: rossella.fonzetti@uniroma3.it*

Declaration of Competing Interests:

The authors acknowledge there are no conflicts of interest recorded.

A B S T R A C T

The triggering of large earthquakes by anthropic activities is a challenging issue in seismology, invoked also for the M_L = 5.9 and 5.8 Emilia 2012 destructive earthquakes. The interaction between the two earthquakes that propagated along adjacent thrusts is still an open issue. In this study, we used waveform cross-correlation and double-difference (DD) location methods to precisely relocate the aftershock sequence and get insights into fault geometry, structure, and rheology by means of DD seismic tomography. Accurate relocations highlight a complex fault system with small-length fault segments coalescing in the Mirandola and Ferrara thrusts. We observe a broad continuous high V_p/V_s anomaly at seismogenic depth (about 6.0 km) that suggests a possible hydraulic connection along the entire fault system. A close look at seismicity indicates a quasi-simultaneous activation of the entire thrust system, with the two mainshocks and large aftershocks occurring within the high V_p/V_s, high fluid-pressure and connecting volume.

1. Introduction

Discriminating the contribution of anthropic activity to the increase of natural hazard is one big challenge. Seismicity induced by underground activity controlled the scientific debate of the past decade (Ellsworth, 2013; Keranen and Weingarten, 2018). Although many direct relations were reported on induced seismic swarms and large events by waste disposal in deep wells (Kim, 2013; Zhang et al., 2013; Baisch and Harjes, 2003; Improta et al., 2015; Goebel et al., 2016), the triggering of earthquakes on critically stressed faults is hard to assess. Stress alteration from geo-energies, such as oil production, may advance the internal clock of faults located in active tectonic regions (Hough et al., 2017). This factor was claimed for the Emilia 2012 destructive earthquakes that originated close to the Cavone oil production site, in northern Italy (Figure 1a, Astiz et al., 2014; Juanes et al., 2016).

In May 2012, an E-W area located at the southern edge of the Po River alluvial plain was hit by a seismic sequence started on the 20th of May with a $M_L = 5.9$ ($M_w = 5.9$, at 02:03:53 UTC), following a $M_L = 4.1$ foreshock occurred 3 hours earlier (Scognamiglio et al., 2012; Govoni et al., 2014). The region was then shaken by thousands of earthquakes, six of them with $M_L \geq 5.0$, including a second main $M_L = 5.8$ ($M_w = 5.7$ at 07:00:03 UTC) earthquake that occurred on May 29th closer to the oil field.

The sequence originated in a seismically active area evidenced by the historical earthquakes (Rovida et al., 2020; Astiz et al., 2014; catalogue CFTI), with the most recent event which occurred about 500 years ago (1570 Ferrara earthquake, $M_e = 5.5$) (Figure 1b).

All large earthquakes show reverse-faulting focal mechanisms, in agreement with the 2-3 mm/yr of compression observed in the area, regionally accommodated by an arcuate fault system buried beneath the plain, forming the broad Ferrara thrust system (Figure 1c, Bennett et al., 2012).

After the first mainshock, the attention was immediately focused on the activity at the nearby Cavone exploitation site, whose production had slowed down for decades. The production of wastewater is compensated with re-injection in a deep well at about 3,300 m depth (Cavone 14, Figure 1a), within the carbonate units hosting the reservoir. Between January 1993 and June 2014, over 3.1×10^6 m^3 of water was injected (Astiz et al., 2014).

Different studies discussed the possible anthropogenic origin of the seismic sequence and reported evidence that changes in stress produced by water disposal in the oil field were small and limited to the immediate proximity of the field (Astiz et al., 2014; Juanes et al., 2016). The small stress changes compared to the large distance between the oil field and the first shock (about 30 km) and the lack of connection between the two ruptured faults and the reservoir were used for arguing against an anthropic contribution.

Based on the spatiotemporal seismicity evolution and the observation of transient velocity changes along the fault system, a high pore pressure pulse at the base of the carbonate multilayer was invoked to explain the triggering of the second mainshock on May 29th (Pezzo et al., 2018). However, there is still no clear evidence for a possible alteration before the first mainshock or a triggering mechanism by fluids, since stress changes due to the field exploitation were negligible at a few km distance from the depth wells (Juanes et al., 2016). A full time-lapse tomography to reveal the eventual changes before the first event is unfeasible due to the lack of data.

Despite the different studies conducted so far, uncertainty on the structural relation and interaction between the two faults remains (Chiarabba et al., 2014). The spatial distribution of the early aftershocks of the sequence (Figure 1a, Table 1) indicates that the western fault (Mirandola thrust) was activated together with the eastern one (Ferrara thrust). This evidence prompted us to closer investigate the crustal volume where the two faults interacted. With this aim, we used revised phase readings, cross-correlation data and double-difference methods to compute high-resolution earthquake locations to refine the fault geometry, yielding new insights into faults' geometrical relation. Then, we computed new velocity models with the *TomoDD* procedure (Zhang and Thurber, 2003) taking advantage of the precise relative locations. Refined V_p and V_p/V_s tomographic models offer new ideas on fluid pressure and hydraulic connectivity along the fault system, useful to explain how the two faults dynamically interacted.

1.1 Geological and seismotectonic outline

The 2012 Emilia seismic sequence struck a portion of the Ferrara arc compressional system, developed in the Late Miocene by the convergence between the European and Adria plates. A series of blind thrusts and related folds involved a sedimentary succession composed of Triassic evaporites, Jurassic-Cretaceous shallow to deep water carbonates and Oligocene-Miocene clastic deposits (Govoni et al., 2014; Astiz et al., 2014; Chiarabba et al., 2014, Figure 1c). A crystalline metamorphic Paleozoic basement is probably located at 8-10 km depth (Bonini et al., 2014). Miocene strata are covered by syntectonic Plio-Pleistocene sandy turbidite and Late Quaternary fluvio lacustrine deposits of the Po valley, with extremely variable thickness (Paolucci et al., 2015).

The Cavone oilfield is characterised by a fold with a moderately dipping (≈ 45°) southern backlimb and a steep dipping forelimb (≥ 60°), bounded to the north by the Mirandola thrust (Astiz et al., 2014). A thickened sequence of the Triassic deposits is located on the hanging wall (Figure 2) suggesting that the Mirandola thrust reactivated an inherited normal fault (Chiarabba et al., 2014).

The May 2012 mainshocks developed on two left-lateral en-echelon blind fault segments dipping to the south: the first mainshock occurred on the central part of the Ferrara thrust and ruptured eastward, the second occurred further west involving the Mirandola thrust (Govoni et al., 2014). Focal solutions show almost pure reverse slip mechanisms (Scognamiglio et al., 2012; Pondrelli et al., 2012), well matching the series of south-dipping planes forming the compressional arc (Figure 1c). Based on 1D and 3D earthquake locations and fault modelling (Pezzo et al., 2018; Juanes et al., 2016), the sequence has been explained as a two-step activation of contiguous fault segments of a more articulated system.

2. Data and Method

In this study, we started from the 1D earthquakes catalogue proposed by *Govoni et al., (2014)*, and later used by *Pezzo et al., (2018)* to compute accurate 3D earthquake locations and V_p and V_p/V_s velocity models. We integrated this dataset with 144 additional seismic events, obtained from the data recorded at the Cavone seismic network. The augmented network consists of 51 three-component weak motion seismic stations, including 4 from Cavone seismic network (blue triangles in Figure 3a); the majority of them are temporary seismic stations installed after the first mainshock of the seismic sequence (red triangles in Figure 3a). The initial catalogue includes 1931 aftershocks, covering a time window between May 20th and June 28th 2012. To increase the resolution of the seismicity catalogue, the seismic events that occurred between 02:03:53 UTC (first mainshock) and 11:55:12 UTC were not used because the distribution of the available seismic stations was not optimal. Thus, the early portion of the seismic sequence has not been relocated.

As a consequence, the location of the first mainshock (on the 20th of May) hails from *Govoni et al. (2014)* (Figure 1a) while the mainshock on the 29th of May comes from double-difference relocation methods.

To improve earthquake locations, we computed high-precision double-difference (DD) relative locations by using the *HypoDD* algorithm (Waldhauser and Ellsworth, 2000) on hand-picked *P*- and *S*-wave arrival times and accurate differential traveltimes computed through waveform cross-correlation (CC) technique.

For all the available data, we computed travel time differences (delay times) for pairs of neighbouring events at common stations using both phase pick data (i.e., high-quality *P* and *S*-wave arrival time readings) and delay-times measured via CC of waveforms coming from correlated earthquakes (earthquakes that occur within 5 km of one another and have similar waveforms; Schaff and Waldhauser, 2005). For each event, we computed phase delay times with the 40 nearest neighbours within a 10 km distance and we selected the 40 highest quality differential times per event pair. Furthermore, we chose only event pairs with at least eight delay times at common stations, in order to guarantee the robustness of the DD inversion process. The final dataset is composed of 508,700 P-wave and 317,605 S-wave delay times computed from the initial high-quality 34,778 P-wave and 22,885 S-wave phase readings.

Simultaneously, we computed CC delay times by using the time domain CC function for large-scale applications described in *Schaff and Waldhauser (2005)*. We applied this method to all the event pairs separated by ≤5 km (based on 3D locations), at all the available stations. We run the CC algorithm on seismograms filtered in the 1–15 Hz frequency range, using a lag time of ±1 s. Correlation measurements are read on two different window lengths for the same phase. In particular, we choose two windows of 0.7 s and 1.4 s for P-waves and 1 s and 2 s for S-waves. The subsequent check of the consistency of the measurements obtained for the two windows reduces the number of outliers due to cycle skipping (Schaff et al., 2004). Thus, we obtained 153,292 P-wave and 327,569 S-wave delay times, having a CC coefficient of 0.8 or larger, that we used in the DD inversion.

In the final step, we combined the CC delay times with hand-picked phase delay times to estimate high-precision relative locations using the algorithm *HypoDD* (Waldhauser and Ellsworth, 2000; Waldhauser and Schaff, 2008). Picks and CC differential times are combined in a dynamically weighted DD inversion. During the iterations, the weighting of cross-correlation and catalogue data delay times has been dynamically adjusted. A 1D velocity model from *Chiarabba et al. (2014)* was used to calculate travel time and partial derivatives. In the first iterations, the absolute pick data were used with full weight, while the CC data were down-weighted (see also Waldhauser, 2001). In the last iterations, the CC data were weighted progressively more than the pick data to improve the relocations. Using this approach, the location precision of correlated seismic events depends on the accuracy of CC data, while unrelated events are controlled by the accuracy of pick data (Waldhauser, 2001). The final DD catalogue includes 1801 seismic events. The map and cross-sections view of the catalogue are shown in Figures 3a and 3b.

As the further step, we use double-difference seismic tomography *TomoDD* code (Zhang and Thurber, 2003) to simultaneously obtain DD relocations of the seismic events and 3D crustal velocity models (V_P and V_S), following the approach applied in many case studies (Zhang et al., 2006; Zhang et al., 2009; Zeng et al., 2016). In the current version of *TomoDD*, the pseudo-bending ray-tracing algorithm

(Um and Thurber, 1987) has been used to trace the ray and for travel-times calculation. Hypocentral and velocity parameters have been computed with the LSQR algorithm. The model is characterised by a regular set of 3D nodes and the velocity values are interpolated by using the trilinear interpolation method (Zhang and Thurber, 2003). The inversion grid nodes (shown in Figure 4, the layer at 6.0 km depth) have a spacing of 5 km in the X and Y directions and of 3 km vertically from 0 to 27 km depth.

The 1D starting velocity model is derived from *Chiarabba et al. (2014)*, and the V_p/V_s was set at 1.90 (see STAB1 in supplementary material). For the inversion, we fixed the maximum velocity change for a node to be less than ± 25-30% of the initial velocity.

Again, we combined cross-correlation and phase reading delay times as input for the inversion procedure. We performed the inversion following the same dynamically weighted inversion scheme used for the *HypoDD* inversion, using the same starting phase and CC delay times used for the *HypoDD* inversion.

We fixed the maximum distance between the cluster centroid and seismic stations at 50 km. We modified the damping parameter, alternating high and low values, in order to stabilise the inversion procedure and to keep the condition number at an acceptable value. In addition, during the iterations, we decided to alternate between earthquake relocations only and simultaneous calculation of velocity and DD relocations. This made the inversion procedure more stable. Furthermore, we optimised the weights of the smoothing along the X, Y and Z directions and fixed the threshold level for DWS (Derivative Weight Sum) at 1000 to invert only the best-sampled volume. The root means square (RMS) of absolute and CC data was progressively reduced.

We first invert the entire P and S wave dataset that consists of 26728 P and 19991 S-wave arrivals (IS1). Then, to obtain a similar resolution for the V_p and V_s models and mitigate artifacts in the V_p/V_s computation, we used a dataset where the number of P and S-wave arrivals are the same (IS2). The number of catalogue P and S delay times (361388 and 235577 respectively) and cross-correlation P and S delay times (23912 and 41217 respectively) are the same in both the inversion procedures to achieve similar earthquake relative locations.

For inversion IS1, the RMS of catalogue data decreased by about 85% from 539 ms to 80 ms; instead, the RMS of CC data was reduced by about 97% from 116 ms to 5 ms. After 17 iterations, *TomoDD* used 89% of absolute data and 57% of CC data. For inversion IS2, the RMS of catalogue data decreased by about 83% from 594 ms to 97 ms; instead, the RMS of CC data was reduced by about 98% from 186 ms to 4 ms. After 17 iterations, *TomoDD* used 84% of absolute data and 54% of CC data. We present and discuss the V_p model obtained by the IS1 inversion, computed with all the P-wave arrivals, and the V_p/V_s model of inversion IS2. The full V_p, V_s and V_p/V_s models of IS2 are reported in the Supplementary material.

3. Results

3.1 Seismicity distribution

High-resolution double-difference aftershocks clearly define the geometry of the two main thrusts (Figure 3a). In order to enhance the imaging of the faults, we show vertical sections perpendicular (sections 1 to 10) and parallel (section 11) to the thrusts system.

Seismicity well defines an about 40-km-long WNW-ESE striking volume including the two main thrusts, highlighting how they might connect at depth. Seismicity occurs between about 5 and 14 km depth, showing a progressive deepening from west to east (Figures 3a and 3b).

The sequence started along the Ferrara thrust (shown in sections 6 to 10 in Figure 3b) with the M_W5.9 20th May mainshock occurring on the shallower portion of the thrust highlighted by the aftershocks (purple star in section 6). High-resolution aftershock locations clearly define a 15-km-long fault plane dipping at low-angle (25 to 30°) to the SW. Seismicity is confined between 5 to 10 km depth for almost the entire fault length, while it deepens up to 14 km depth at the eastern termination of the fault (section

10 in Figure 3b). The fault plane shows a simple almost-planar geometry in its central portion (sections 6 and 7), while it shows a more complicated geometry at the eastern termination (sections 8 and 9).

Just 3 minutes after the M_W5.9 20th May mainshock (Table 1), seismicity surged on the Mirandola fault to the west (sections 1 to 5 in Figure 3b) with a M_L4.8 earthquake (yellow star in section 4 in Figure 3b). The largest earthquake is the M_W5.7 second mainshock of 29th May located at the deepest tip of the fault portion defined by aftershocks (purple star in section 4), that define a 20-km-long fault plane dipping to SW, steeper than the Ferrara thrust (35 - 40°).

Sections 4 and 5 show the transition zone between the two thrust faults. Seismicity is less clustered, compared to the two almost planar thrusts, defining a volume where the two main planes are intersecting. In this portion of the fault system, small-scale (about 1-km-long) fault segments link the two adjacent faults.

Section 11 is parallel to the strike of the two faults showing events occurring within +/-6 km from the cross-section. Seismicity highlights the different depths of the two main thrusts involved: the Mirandola thrust (western portion of section 11) develops approximately between 5-10 km depth, while the Ferrara thrust (eastern portion) is deeper, with events occurring between 5 up to 15 km depth. The overall seismicity distribution suggests that the two adjacent faults are connected at the base of the seismogenic zone along the low-angle Ferrara thrust.

3.2 Model reliability

To define the model resolution, we computed synthetic tests, creating a velocity model and compared the model reproducibility with the Spread Function (SF) computed by means of Simulps14 (as defined in *Toomey and Foulger, 1989).* We fixed a value of SF = 2, indicative of compact averaging vectors and resolution picked on the diagonal element and plotted the contour in the following figure (Figure 4-8).

Furthermore, the resolution of the model is also addressed by the reproducibility of a synthetic 3D input model through which travel times have been computed (Merrill et al., 2022). We first computed a standard checkerboard test. We used the same event and station locations as in the analysis of the real data and create a model perturbed, alternating a variation of ±5% at each node of the layers. This pattern of perturbation is present in both the V_p and V_p/V_s models.

Figure 4 shows the results of the checkerboard test, computed using the original absolute P- and S-waves travel times (IS1). The resolution decreases with depth, as confirmed by the pattern of the SF. The original perturbations are well reproduced at 6, 9, and 12 km depth. Furthermore, we compute a restore test, in which the synthetic feature is the final model obtained from the inversion (see SOM1 in the supplementary material). The features are well reproduced both in V_p and V_p/V_s in layers at 6, 9, and 12 km depth. The central portion of the model, i.e., the volume discussed in the paper, is well resolved, as indicated by the SF and tests reproducibility.

3.3 Velocity models

3.3.1 *TomoDD velocity models*

Velocity models present strong lateral heterogeneities (Figure 5). The V_p ranges from less than 4 km/s at 3 km depth, to 6–7 km/s at 12 km depth, values slightly lower than those in *Chiarabba et al., 2014*. The V_p/V_s ranges from 1.80 to 2.00. Most of the aftershocks are located between 5 to 10 km depth, within a high V_p and high V_p/V_s anomalous body (Figure 5).

At 3 km depth, very few aftershocks occur in the portion characterised by relatively high V_p (about 4.0 km/s). A high V_p/V_s area is visible, along the Mirandola and Ferrara thrust faults, where $M_L \geq 4$

aftershocks are located. The area of Cavone 14 injection well is characterised by a low V_s (Figure 6; see auxiliary material for the 3D V_s model of IS2, SOM3a), that is consistent with the presence of high fluid pressure within the oilfield volume.

At 6 km, the pattern of the V_p and V_p/V_s models identifies the extent of the carbonate units (Chiarabba et al., 2014; Valoroso et al., 2013; see Figure 1c). A laterally continuous high V_p anomaly extends between the two mainshocks. Between the two thrusts, a low V_s zone, with values ranging from 3.0 to 2.5 km/s, is evident (Figure 6 and SOM3a, at 6 km depth), suggesting the presence of an intensely fractured volume, part of a broad extended fluid-filled carbonate volume. Most of the seismicity is concentrated at the border of the carbonate volume, and at the highest gradient of V_p/V_s, suggesting an active role of high-pressure fluids in controlling earthquake occurrence. We observe a smaller V_s velocity close to Cavone oilfield, consistent with high fluid pressure.

At 9 km depth, the central high V_p, high V_p/V_s anomaly is still present, and aftershocks are located within either high or low V_p/V_s volumes. At 12 km depth, the central portion has low V_p and low V_p/V_s anomalies suggesting the presence of the metamorphic Paleozoic basement (Carminati et al., 2010; Chiarabba et al., 2014) that underlies the sedimentary cover.

In Figure 7, vertical sections of the tomographic model across the epicentral area help the imaging of the segments of the thrust system. The ruptured faults entirely lay within the sedimentary cover and do not seem to propagate within the metamorphic Paleozoic basement. In sections 1 and 2, velocity anomalies help in defining the Mirandola thrust fold anticline. All aftershocks occur proximally to the border of a high V_p/V_s zone. Aftershock alignment defines the Mirandola thrust at a clear velocity contrast. The 29th May mainshock (pink star) originated within a strong V_p/V_s contrast at the base of the high-velocity body (Section 4), while the aftershocks occurred within a high V_p/V_s area. Seismicity aligns along the southwest dipping thrust limiting the structural high, produced by the buried fold system (Figure 1c, Bonini et al., 2014).

From west to east (sections 1, 2, 4 in Figure 7), the positive structure forming the main folds of the sedimentary cover is well evident down to 10 km depth. High V_p/V_s values are concentrated in the upper portion of the fold, confirming the presence of fluids within the Mirandola structure, which hosts the Cavone oilfield reservoir (Astiz et al., 2014). The lateral continuity of the V_p anomalies and the relative position of aftershocks in sections 4 and 6 indicate that the Mirandola and Ferrara thrusts are connected, forming a broad high-velocity sedimentary structure deformed by compression. Sections 4 and 5 show the transition zone between the main thrusts. In this portion of the fault system, small-scale (about 1-km-long) fault segments link the two adjacent faults, connecting them to the base of the seismogenic zone along a low-angle deeper thrust defined by the overthrusting of the high V_p carbonate volume onto deeper lower V_p. The sparser distribution of aftershocks on these two sections probably results from the interference with the presence of steep splays and back trusts, as hypothesised for the formation of the Mirandola and Ferrara thrust units (Figures 1c and 7, Carminati et al., 2010). The first 20th May 2012 mainshock nucleates within a high V_p, high V_p/V_s zone. A deep low V_p anomaly is observed at the base of the two thrusts (sections 1 and 6 in Figure 7). Velocity perturbations are in the range of -/+20%, with strongly positive values in the deeper portions of the crust (i.e., greater than 10 km depth, see SOM4). The majority of events are concentrated in areas with positive velocity anomalies. In some spots of the fault system, the V_p/V_s anomaly is higher than the V_p anomaly for the significant variation of the S- wave velocity (see sections 1, 2 and 6 in supplementary material, SOM4).

Figure 8 shows the V_p and V_p/V_s models almost parallel to the average strike of the two thrusts (same section 11 as in Figure 3a). All the aftershocks with larger magnitude occur in a volume characterised by high V_p/V_s ratio or close to a zone characterised by a strong V_p/V_s velocity contrast. A continuous very high V_p/V_s body with V_p = 6 km/s extends from 6 to 9 km depth. The portion near the main aftershock (yellow star) is characterised by a low V_s velocity and a high V_p/V_s value, highlighting an area with high-pressure fluids.

3.3.2 Comparison with the previous model

Before discussing our new results, we compared them with tomographic models computed with similar data but different methods (*Chiarabba et al., 2014)*. The V_p models are similar to a great length, with the V_p absolute values a bit lower than in the previous model. The V_p/V_s models are similar in the deeper layers; instead, they differ at 3.0 and 6.0 km depth, in terms of the vertical and lateral extent of the high V_p/V_s anomaly (see SOM2). Such differences can arise from the different approach used for estimating V_p/V_s. In the previous model, V_p/V_s parameters are directly inverted by using S-P times. The main advantage is that a smaller number of S-wave arrival times can be handled, but S-wave rays are not traced. In our study, P- and S- wave arrival times are computed from V_p and V_s models, and S-wave rays are traced. The different number of data and the resolution might introduce a bias in the V_p/V_s computation, but our approach (IS2) mitigates such artifacts. The observed differences in velocity results can derive from the different solutions of the location-velocity coupling, inversion approach, model regularisation, and ray tracing of S-waves between the two methods.

4. Discussion

The role of fluids in triggering earthquakes and varying seismicity rates is a hot topic. The principal process is the effective normal stress reduction on the fault, with lubrication that yields a rapid propagation of seismic ruptures (Scuderi and Collettini, 2016; Cornelio et al., 2019). Although the frictional weakening of faults at elevated pore pressure has been observed in laboratory experiments (Scuderi et al., 2017; Wang et al., 2020), evidence from natural events is still mostly indirect (Chiarabba et al., 2014).

The stress alteration by reinjection of wastewater in fossil fuel production within a reservoir led to changes in seismicity rates at a local and regional scale and triggering of even large events (Ellsworth, 2013; Brodsky and Lajoye, 2013; Keranen et al., 2014; Buttinelli et al., 2016). In this general context, the 2012 Emilia earthquakes are a relevant case for understanding if and how anthropic activities can trigger destructive events of such a kind. Thanks to a long history of production data (Astiz et al., 2014), the stress alteration generated by exploitation at the Cavone oil field has been modelled, following a coupled flow-geomechanics approach (Juanes et al., 2016). The computed Coulomb stress changes are small close to the injection well and become negligible at the distance of the first mainshock hypocenter. Modelling supported the idea that exploitation was not a driver of seismicity, although pore pressure migration within highly heterogeneous and fractured crustal material is complex to model.

In this study, we have refined the characteristics of the volume along the fault system in terms of elastic parameters and relation with the activated faults. High-resolution relocated aftershocks and tomograms might give hints for unravelling the structural features of the area that consist of a folded sedimentary cover (Figure 1c) with active north-east verging thrusts that splay from a main low-angle basal plane (Figures 3, 5 and 7).

The strongest V_p contrast is related to this deeper and flatter fault that might represent the main plane of shortening. The Mirandola fault is shallower (5 to 10 km depth range) and steeper (35-40° dip), located at the border of a high V_p/V_s, high fluid pressure volume in the hanging wall of the main plane. The Ferrara thrust is the eastward continuation of the main plane and lies in a volume with a high V_p/V_s contrast. The two faults are connected in a small volume where they splay one from the other, at a distance of 15-18 km from the injection well (see layers at 3 and 6 km depths in Figure 5). Our results emphasise the geometry of the thrusts, both activated at the onset of the seismic sequence within a few minutes from one another (sections 4 and 5 in Figure 7).

The 3D V_s model permits to focus on the role of fluids along the fault system (Figure 6 and SOM3a, 6 km depth layer). Near the major aftershocks of 29th May (yellow stars in the west) and the connection zone of the two thrusts, a high V_p/V_s and low S-wave velocities (from 3.5 km/s to 2.5 km/s) might indicate a local overpressure of fluids within the sedimentary units. While the main features of the V_p model are similar to those computed with other inversion methods (Chiarabba et al., 2014; Pezzo et al., 2018), some significant details are revealed here, most strikingly for the V_p/V_s model. A continuous high V_p anomaly ($V_p > 6.0$ km) marks the base of the sedimentary cover consisting of a thick layer of dolomites (Astiz et al., 2014). This body, locally interrupted beneath the western part of the Cavone reservoir, is continuous in the crustal portion between the Cavone 14 injection well and the two mainshock hypocenters. A similarly elongated high V_p/V_s anomaly suggests high pore fluid pressure within this body. The lateral continuity of V_p and V_p/V_s might indicate a hydraulic connection at the base of the carbonate multilayer along the entire fault system. Tomograms and aftershock distribution highlight that the seismic sequence started on the Ferrara thrust and then ruptured almost simultaneously the adjacent Mirandola thrust, in a junction portion where small-scale segments are coalescing on a single larger fault (sections 4 and 5 in Figure 3b) along which the second mainshock originated nine days later.

The majority of aftershocks in the volume portion between the reservoir and the two mainshocks occur within such high V_p/V_s volumes, in response to the high pore pressure (Zhao et al., 2015; Dvorkin et al., 1999; Takei, 2002; Nur, 1972). The fault segment activated on May 20th is located predominantly in low V_p/V_s volumes, except for the hypocenter that is indeed located within the same high V_p/V_s, high fluid pressure central volume. The sharp bound of seismicity to the west coincides with a lineament that is intersecting the main thrust faults, suggesting fluid compartments segmented by pre-existing faults within the carbonate volumes.

The almost simultaneous activation of the two thrusts, being the first event on the second (Mirandola) fault occurred only a few minutes after the first mainshock (Table 1), suggests a dynamic interaction between the two faults, where stress changes are rapidly transferred. The rupture of the first event on a low V_p/V_s, an unpressured portion of the system well matches the relatively smaller number of aftershocks and the missed eastward migration of the sequence.

5. Conclusions

In this study, we compute new tomograms to help a more clear definition of the geometry of the Mirandola and Ferrara thrusts, seismic sources activated during the 2012 Emilia seismic sequence. High-resolution earthquake locations show that the Mirandola thrust is shallower and steeper than the Ferrara thrust, being adjacent splays of a larger flat-ramp-flat structure (Figures 3, 5-8). The almost simultaneous activation of the two adjacent segments by the first mainshock and by a M_L 4.8 event that occurred a few minutes later suggests a dynamic interaction between the two segments. The two mainshock hypocenters are located within a high V_p/V_s, high fluid pressure volume, hydraulically connected and floored by a low V_p and low V_p/V_s basal shear zone.

Data and Resources

Historical seismicity comes from: catalogue CFTI (http://storing.ingv.it/cfti.4med/, CPTI15-DMBI15-v4.0, https://emidius.mi.ingv.it/CPTI15-DBMI15/). The instrumental seismicity comes from http://terremoti.ingv.it/. Waveforms data recorded by the INGV permanent and temporary networks are available at the INGV node of the European Integrated Data Archive: https://eida.ingv.it/it/ . The Ferrara and Mirandola thrusts come from DISS 3.3.0: Database of Individual Seismogenic Sources - https://diss.ingv.it/diss330/dissmap.html. The 1D starting earthquake locations come from *Govoni et al., 2014.* Figures are generated by the Generic Mapping Tools (GMT) by Wessel et al., 2019 (https://doi.org/10.1029/2019GC008515).

Supplemental Material for this article includes:

- STAB1: 1D starting velocity model from Chiarabba et al., 2014.
- SOM1: recovery test. The real dataset came from IS2 (absolute data modified, as described in paragraph 2, to obtain a V_p/V_s ratio which takes into account S-wave contribution);
- SOM2: comparison between the previous model and the new combined model obtained with IS1 and IS2;
- SOM3: The 3D V_p, V_s and V_p/V_s models obtained with IS2;
- SOM4: 3D V_p (from IS1) and V_p/V_s (from IS2) velocity anomalies of the cross sections, shown in Figure 6.

Acknowledgments

We are indebted to Marco Calò for his suggestions and advice on TomoDD software. We are grateful to the two anonymous reviewers and the Editor for constructive comments which improved our work.

References

Astiz, L., Dieterich, J. H., Frohlich, C., Hager, B. H., Juanes, R., and J. H. Shaw (2014). *On the potential for induced seismicity at the Cavone oilfield: Analysis of geological and geophysical data, and geomechanical modeling*. Report for the Laboratorio di Monitoraggio Cavone (139 pp.). Retrieved from http://labcavone.it/documenti/32/allegatrapporto-studiogiacimento.pdf

Baisch, S., and H. P. Harjes (2003). *A model for fluid-injection-induced seismicity at the KTB, Germany*. Geophys. J. Int. 152.1 (2003), 160–170.

Bennett, R. A., Serpelloni, E., Hreinsdòttir, S., Brandon, M.T., Buble G., Basic, T., Casale, G., Cavaliere, A., Anzidei, M., Marjonovic, M., Minelli, G., Molli G., and A. Montanari (2012). *Syn-convergent extension observed using the RETREAT GPS network, northern Apennines, Italy.* J. Geophys. Res, vol. 117, B04408, doi:10.1029/2011JB008744, 2012.

Bonini, L., Toscani, G., and S. Seno (2014). *Three-dimensional segmentation and different rupture behavior during the 2012 Emilia seismic sequence (Northern Italy).* Tectonophysics, vol. 630, https://doi.org/10.1016/j.tecto.2014.05.006.

Brodsky, E.E., and L.J. Lajoie (2013). *Anthropogenic seismicity rates and operational parameters at the Salton Sea Geothermal Field*. Science, 341, 6145, 543-546.

Buttinelli, M., Improta, L., Bagh S., and C. Chiarabba (2016). *Inversion of inherited thrusts by wastewater injection induced seismicity at the Val d'Agri oilfield (Italy).* Scientific RepoRts | 6:37165 | DOI: 10.1038/srep37165.

Castello, B., Selvaggi, G., Chiarabba, C., Amato, A. (2006). *CSI Catalogo della sismicità italiana 1981-2002, versione 1.1. INGV-CNT, Roma.* DOI: 10.13127/CSI.1.1.

Carminati, E., Scrocca, D., and C. Doglioni (2010). *Compaction-induced stress variations with depth in an active anticline: Northern Apennines, Italy.* J. Geophys. Res. 115 (B02401). http://dx.doi.org/10.1029/2009JB006395

Chiaraluce, L., Chiarabba, C., Collettini, C., Piccinini, D., and M. Cocco (2007). *Architecture and mechanics of an active low-angle normal fault: Alto Tiberina Fault, northern Apennines, Italy.* J. Geophys. Res, vol. 112, B10310, doi:10.1029/2007JB005015, 2007.

Chiarabba, C., De Gori, P., Improta, L., Lucente, F. P., Moretti, M., Govoni, A., Di Bona, M., Margheriti, L., Marchetti, A., and A. Nardi (2014). *Frontal compression along the Apennines thrust system: The Emilia 2012 example from seismicity to crustal structure.* J. Geodyn., http://dx.doi.org/10.1016/j.jog.2014.09.003 .

Cornelio, C., Spagnuolo, E., Di Toro, G., Nielsen, S., and M. Violay (2019). *Mechanical behaviour of fluid - lubricated faults.* Nature Communications, 10(1), 1274. https://doi.org/10.1038/s41467- 019-09293- 9

Dvorkin, J., Mavko, G., and A. Nur (1999). Overpressure detection from compressional- and shear wave data: Geophysical Research Letters, v. 26, p. 3417–3420, doi: 10.1029/1999GL008382.

Ellsworth, W. L. (2013). *Injection–Induced earthquakes*. Science, Vol 341, 6142. DOI: 10.1126/science.1225942.

Goebel, T. H. W., Hosseini, S. M., Cappa, F., Hauksson, E., Ampuero, J. P., Aminzadeh, F., and J. B. Saleeby (2016). *Wastewater disposal and earthquake swarm activity at the southern end of the Central Valley, California.* Geophysical Research Letters, 43(3), 1092–1099, https://doi.org/10.1002/2015GL066948

Govoni, A., Marchetti, A., De Gori, P., Di Bona, M., Lucente, F. P., Improta, L., Chiarabba, C., Nardi, A., Margheriti, L., Agostinetti, N. P., Di Giovambattista, R., Latorre, D., Anselmi, M., Ciaccio, M. G., Moretti, M., Castellano, C. and D. Piccinini (2014). *The 2012 Emilia seismic sequence (Northern Italy): Imaging the thrust fault system by accurate aftershock location*. Tectonophysics, http://dx.doi.org/10.1016/j.tecto.2014.02.013 .

Hough, S.E., Tsai, V.C., Walker, R, and F. Aminzadeh (2017). *Was the* M_w *7.5 1952 Kern County, California, earthquake induced (or triggered)?.* J Seismol. 2017;21(6):1613-1621. doi: 10.1007/s10950-017-9685-x. Epub 2017 Oct 2. PMID: 29200935; PMCID: PMC5693966.

Improta, L., Valoroso, L., Piccinini, D., and C. Chiarabba (2015). *A detailed analysis of wastewater-induced seismicity in the Val d'Agri oilfield (Italy).* Geophys. Res. Lett.,42, 2682–2690, doi:10.1002/2015GL063369.

Juanes, R., Jha, B., Hager, B. H., Shaw, J. H., Plesch, A., Astiz, L., Dieterich, J. H., and C. Frohlich (2016). *Were the May 2012 Emilia-Romagna earthquakes induced? A coupled flow-geomechanics modelling assessment*. Geophys. Res. Lett., 43, 6891–6897, doi:10.1002/2016GL069284.

Keranen, K. M., and M. Weingarten (2018). *Induced seismicity.* Annu. Rev. Earth Planet. Sci. 2018. 46:149–74. https://doi.org/10.1146/annurev-earth-082517-010054.

Kim W. Y. (2013). *Induced seismicity associated with fluid injection into a deep well in Youngstown, Ohio.* Journal of Geophysical Research: Solid Earth, vol. 118, 3506–3518, doi:10.1002/jgrb.50247, 2013.

Merrill, R. J., Bostock, M. G., Peacock, S. M., Schaeffer, A. J., and S. W. Roecker (2022). *Complex structure in the Nootka Fault zone revealed by double-difference tomography and a new earthquake catalog.* Geochemistry, Geophysics, Geosystems, 23, e2021GC010205. https://doi.org/10.1029/2021GC010205

Nur, A. (1972). Dilatancy, pore fluids, and premonitory variations of Ts/Tp travel times: Bulletin of the Seismological Society of America, v. 62, p. 1217–1222.

Pezzo, G., De Gori, P., Lucente, F. P., and C. Chiarabba (2018). *Pore Pressure Pulse Drove the 2012 Emilia (Italy) Series of Earthquakes*. Geophysical Research Letters, 45. https://doi.org/10.1002/2017GL076110.

Pondrelli, S., Salimbeni, S., Perfetti, P., and P. Danecek (2012). *Quick regional centroid moment tensor solutions for the Emilia 2012 (northern Italy) seismic sequence.* Ann. Geophys. 55 (4), 599–607, http://dx.doi.org/10.4401/ag-6146.

Rovida, A., Locati, M., Camassi, R., Lolli, B., and P. Gasperini (2020). *The Italian earthquake catalogue CPTI15.* Bulletin of Earthquake Engineering (2020) 18:2953–2984 https://doi.org/10.1007/s10518-020-00818-y .

Scognamiglio, L, Margheriti, L., Mele, F.M., Tinti, E., Bono, A., De Gori, P., Lauciani, V., Lucente, F.P., Mandiello, A. G., Marcocci, C., Mazza, S., Pintore, S., and M. Quintiliani (2012). *The 2012 Pianura Padana Emiliana seismic sequence: locations, moment tensors and magnitudes.* Ann. Geophys. 55 (4), 549–559. http://dx.doi.org/10.4401/ag-6159 .

Schaff, D. P., and F. Waldhauser (2005). *Waveform Cross-Correlation-Based Differential Travel-Time Measurements at Northern California Seismic Network.* Bulletin of the Seismological Society of America, Vol. 95, No. 6, pp. 2446–2461, December 2005, doi: 10.1785/0120040221.

Scuderi, M. M., Collettini, C., and C. Marone (2017). *Frictional stability and earthquake triggering during fluid pressure stimulation of an experimental fault.* Earth and Planetary Science Letters, 477, 84–96. https://doi.org/10.1016/j.epsl.2017.08.009

Scuderi, M. M., and C. Collettini (2016). *The role of fluid pressure in induced vs. triggered seismicity: insights from rock deformation experiments on carbonates.* Scientific Reports, 6(1), 1. Retrieved from–9. https://doi.org/10.1038/srep24852.

Takei, Y. (2002). Effect of pore geometry on Vp/Vs: From equilibrium geometry to crack: Journal of Geophysical Research, v. 107, doi: 10.1029/2001JB000522.

Toomey, D.R. and G.R. Foulger (1989). *Tomographic Inversion of Local Earthquake Data From the Hengill-Grensdalur Central Volcano Complex, Iceland.* Journal of Geophysical Research; Vol., 94, pages 17,497-17,510, https://doi.org/10.1029/JB094iB12p17497.

Um, J., and C.H. Thurber (1987). *A fast algorithm for two-point seismic ray tracing.* Bull. Seism. Soc. Am. 77, 972–986.

Valoroso, L., Chiaraluce, L., Piccinini, D., Di Stefano, R., Schaff, D., and F. Waldhauser (2013). *Radiography of a normal fault system by 64,000 high-precision earthquake locations: The 2009L'Aquila (central Italy) case study.* Journal of Geophysical Research; Solid Earth, Vol., 118, 1–21, doi:10.1002/jgrb.50130, 2013.

Waldhauser, F., and W. L. Ellsworth (2000). *A Double-Difference Earthquake Location Algorithm: Method and Application to the Northern Hayward Fault, California.* Bulletin of the Seismological Society of America, 90, 6, pp. 1353–1368, December 2000.

Waldhauser, F. (2001). *hypoDD: A Program to Compute Double-Difference Hypocenter Locations (hypoDD version 1.0 - 03/2001)*. U.S. Geol. Survey, Open File Report 01-113.

Waldhauser, F., and D. P. Schaff (2008). *Large-scale relocation of two decades of Northern California seismicity using cross-correlation and double-difference methods.* Journal of Geophysical Research, vol. 113, B08311, doi:10.1029/2007JB005479, 2008.

Wang, L., Kwiatek, G., Rybacki, E., Bonnelye, A., Bohnhoff M., and G. Dresen (2020). *Laboratory study on fluid‐induced fault slip behavior: The role of fluid pressurization rate.* Geophysical Research Letters, 47, e2019GL086627. https://doi.org/10.1029/2019GL086627

Wessel, P., Luis, J.F., Uieda, L., Scharroo, R., Wobbe, F., Smith, W.H.F., and D. Tian (2019). The Generic Mapping Tools version 6. Geochem. Geophys. Geosyst., vol. 20, https://doi.org/10.1029/2019GC008515

Zeng, X., Thurber, H. C., Shelly, D. R., Harrington, R. M., Cochran, E. S., Bennington, N. L., Peterson, D., Guo, B., and K. McClement (2016). *3-D P- and S-wave velocity structure and low-frequency earthquake locations in the Parkfield, California region.* Geophys. J. Int. (2016) 206, 1574–1585 doi: 10.1093/gji/ggw217.

Zhang, H., and C. H. Thurber (2003). *Double-Difference Tomography: The Method and Its Application to the Hayward Fault, California.* Bulletin of the Seismological Society of America, Vol. 93, No. 5, pp. 1875–1889, October 2003.

Zhang, H., and C. Thurber (2006). Development and applications of double-difference seismic tomography. Pure and Applied Geophysics, 163(2), 373-403.

Zhang, H., Thurber, C. H., and P. Bedrosian (2009). *Joint inversion for Vp, Vs, and Vp/Vs at SAFOD, Parkfield, California.* Geochem. Geophys. Geosyst., 10, Q11002, doi:10.1029/2009GC002709.

Zhang, Y., Person, M., Rupp, J., Ellett, K., Celia, M. A., Gable, C. W., Bowen, B., Evans, J., Bandilla, K., Mozley, P., Dewers, T., and T. Elliot (2013). *Hydrogeologic controls on Induced Seismicity in Crystalline Basement Rocks Due to Fluid Injection into Basal Reservoirs.* Vol. 51, No. 4– Groundwater–July-August 2013 (pages 525–538).

Zhao, D., Kitagawa, H., and G. Toyokuni (2015). A water wall in the Tohoku forearc causing large crustal earthquakes. *Geophysical Journal International*, *200*(1), 149-172.

Full mailing addresses:

Fonzetti R.

Istituto Nazionale di Geofisica e Vulcanologia (INGV)

Via Vigna Murata 605 (00143), Rome (Italy)

rossella.fonzetti@ingv.it

Dipartimento di Scienze della Terra

Università degli Studi Roma Tre

Largo S. Leonardo Murialdo 1 (00146), Rome (Italy)

rossella.fonzetti@uniroma3.it

Valoroso L.

Istituto Nazionale di Geofisica e Vulcanologia (INGV)

Via Vigna Murata 605 (00143), Rome (Italy)

luisa.valoroso@ingv.it

De Gori P.

Istituto Nazionale di Geofisica e Vulcanologia (INGV)

Via Vigna Murata 605 (00143), Rome (Italy)

pasquale.degori@ingv.it
Chiarabba C.
Istituto Nazionale di Geofisica e Vulcanologia (INGV)
Via Vigna Murata 605 (00143), Rome (Italy)
claudio.chiarabba@ingv.it

Tab. 1: The mainshock of 20th May 2012 and the aftershocks occurring a few minutes later (from Govoni et al., 2014).

Fig. 1: a) Map view of the seismicity recorded during the first day of the 2012 Emilia seismic sequence. Earthquakes are colour-coded according to their time occurrence. The dots are aftershocks with $M_L < 4.0$*. The bigger stars are the mainshocks of 20th May (black) and 29th May 2012 (pink), while the smaller stars are the aftershocks with* $M_L \geq 4.0$*. The Cavone oilfield is shown: the black squares represent the location of wells and the red one is the Cavone14 injection well. The red line is the section visible in Figure 1c. The pink rectangle indicates the 2D extension of the Cavone oilfield. Blue and pink lines represent the Ferrara and Mirandola thrust fronts, respectively. The black bold box emphasises the study area. The black arrows represent the stress field of the study area. The grey area is the Apennines foredeep; b) Distribution of seismicity between 1200 to July 2022. The squares are the historical earthquakes, with dimensions scaled according to magnitude. Dots are the instrumental seismicity coming from CSI-1.1 (Castello et al., 2006) and INGV website. The red line represents the B'- B section in Figure 2. c) Cross section showing the geometry of the thrust system with the main units (modified from Bonini et al., 2014).*

Fig. 2: The interpretation of the seismic reflection profile B-B' shows the geometry of the Mirandola thrust and the mechanism of fault propagation fold. The yellow dots are the aftershocks localised in Astiz et al., 2014 (Modified from Astiz et al., 2014).

Fig. 3: a) Double-difference locations of the 2012 Emilia seismic sequence. Blue triangles represent the seismic stations of the Cavone oil field, while red triangles and grey squares represent temporary and permanent stations managed by INGV respectively. Pink stars are the mainshocks of the 20th and 29th of May 2012. Yellow stars are the aftershocks with $M_L \geq 4$. Black dots are the aftershocks with $M_L < 4$ that occurred in the period between 20/05/2012 – 28/06/2012. The pink and blue lines are the Ferrara and Mirandola thrusts respectively. The black lines are the traces of vertical sections shown in figure 3b: sections 1 to 5 are striking 15°N, while sections 6 to 10 are striking 20°N; b) Vertical cross-sections show the depth-distribution of the aftershocks occurring within +/- 2.0 km distance from the cross-section for sections 1-10, and +/- 6.0 km for section 11. The red lines are the interpreted thrust planes highlighted by the relocated events.

Fig. 4: Checkerboard test, perturbing all layers of the V_p and V_p/V_s models. The pink line is the Spread Function (SF$\leq$2). The black crosses represent the grid used for TomoDD inversions. For each black box: above, the final model obtained by inverting synthetic data; below, the synthetic model perturbed.

Fig. 5: P-wave velocity and V_p/V_s models in the four inverted layers. High V_p/V_s anomalies are evidenced. The pink line is the Spread Function (SF $\leq$2). Hypocenters of the relocated events are reported in the respective layers. Pink stars indicate the mainshocks of the 20th and 29th May 2012; yellow stars represent the aftershocks of the 2012 Emilia seismic sequence, with $M_L \geq 4.0$. The white dots indicate the aftershocks with $M_L < 4.0$. Aftershocks come from TomoDD relocations. In the 3 km depth layer, the used grid is represented by black crosses. Grey lines are the main thrusts involved in the 2012 Emilia seismic sequence.

Fig. 6: 3D V_p, V_s and V_p/V_s at 6 km depth (IS2 model) and relocated aftershocks. The light brown dashed line indicates the area with a high V_p/V_s. The pink line is the Spread Function (SF$\leq$2). Pink stars are the mainshocks of 20th and 29th May 2012. Yellow stars are the aftershocks with $M_L \geq 4.0$. White dots represent the aftershocks with $M_L < 4.0$. The Cavone14 oil well is shown.

Fig. 7: Vertical sections of P-wave and V_p/V_s models obtained with TomoDD inversions IS1 and IS2. The pink line is the Spread Function (SF≤ 2). White lines indicate the basal thrust. Pink stars are the mainshocks of 20th and 29th May 2012. Yellow stars are the aftershocks with $M_L \geq 4.0$. White dots represent the aftershocks with $M_L < 4.0$. The Cavone14 oil well is shown in section 1. Earthquakes occurring within +/- 2 km from the vertical sections are shown.

Fig. 8: Vertical section of V_p and V_p/V_s models along the fault system. The pink line is the Spread Function (SF≤ 2). The black boxes are the main thrusts (Mirandola and Ferrara). The red box is the connection zone between the two mainshocks (pink stars). The yellow stars and white dots are relocated aftershocks with $M_L \geq 4.0$. and $M_L < 4.0$, respectively. The Cavone14 oil well is shown. Earthquakes occurring +/- 6 km from the vertical section are shown.

Figure1

a)

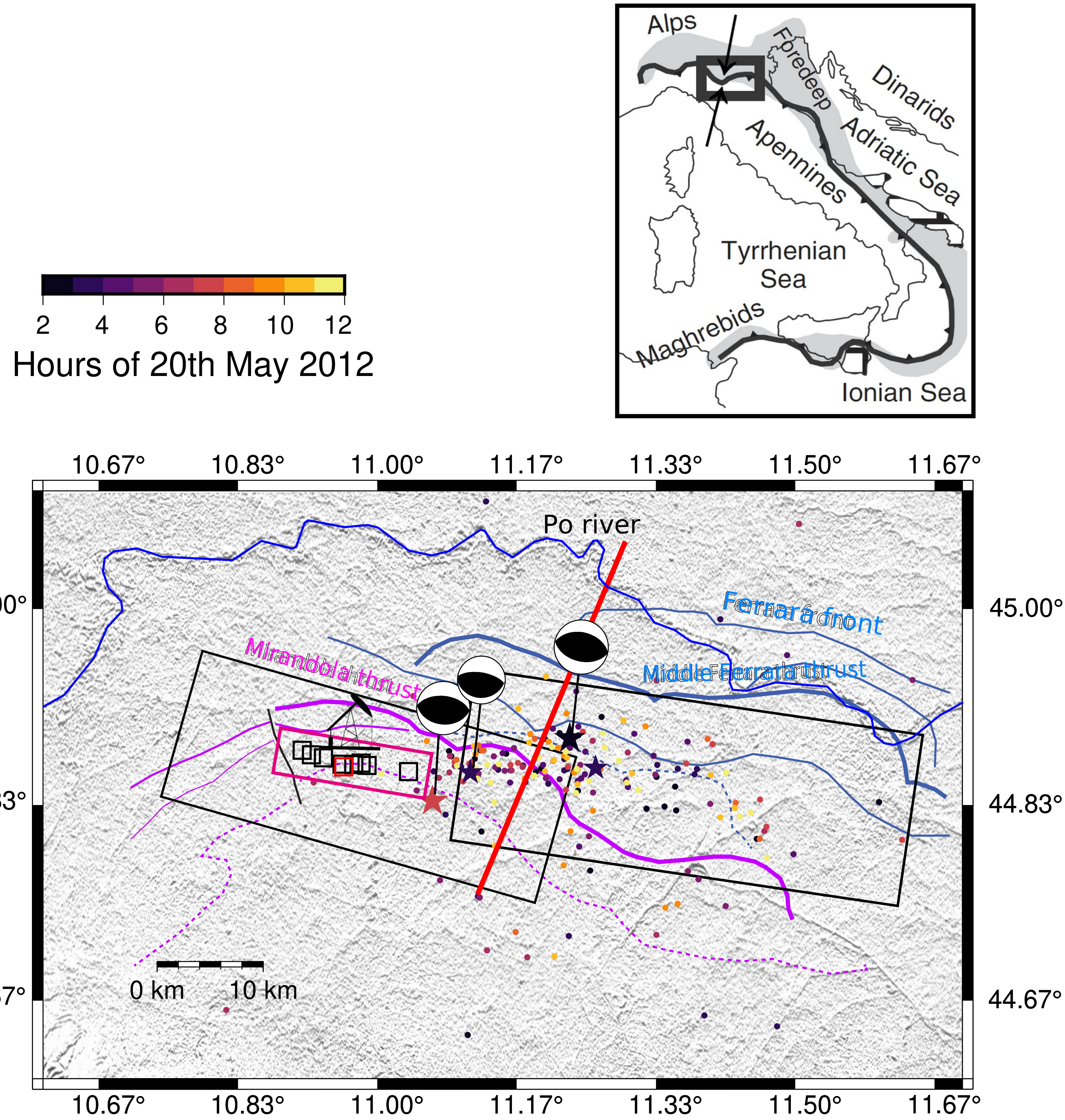

2
4
6
8
10
12
Hours of 20th May 2012
Alps
Foredeep
Dinarids
Adriatic Sea
Apennines
Tyrrhenian
Sea
Maghrebids
Ionian Sea
10.67°
10.83°
11.00°
11.17°
11.33°
11.50°
11.67°
45.00°
44.83°
44.67°
Po river
Ferrara front
Middle Ferrara thrust
Mirandola thrust
0 km
10 km

b)

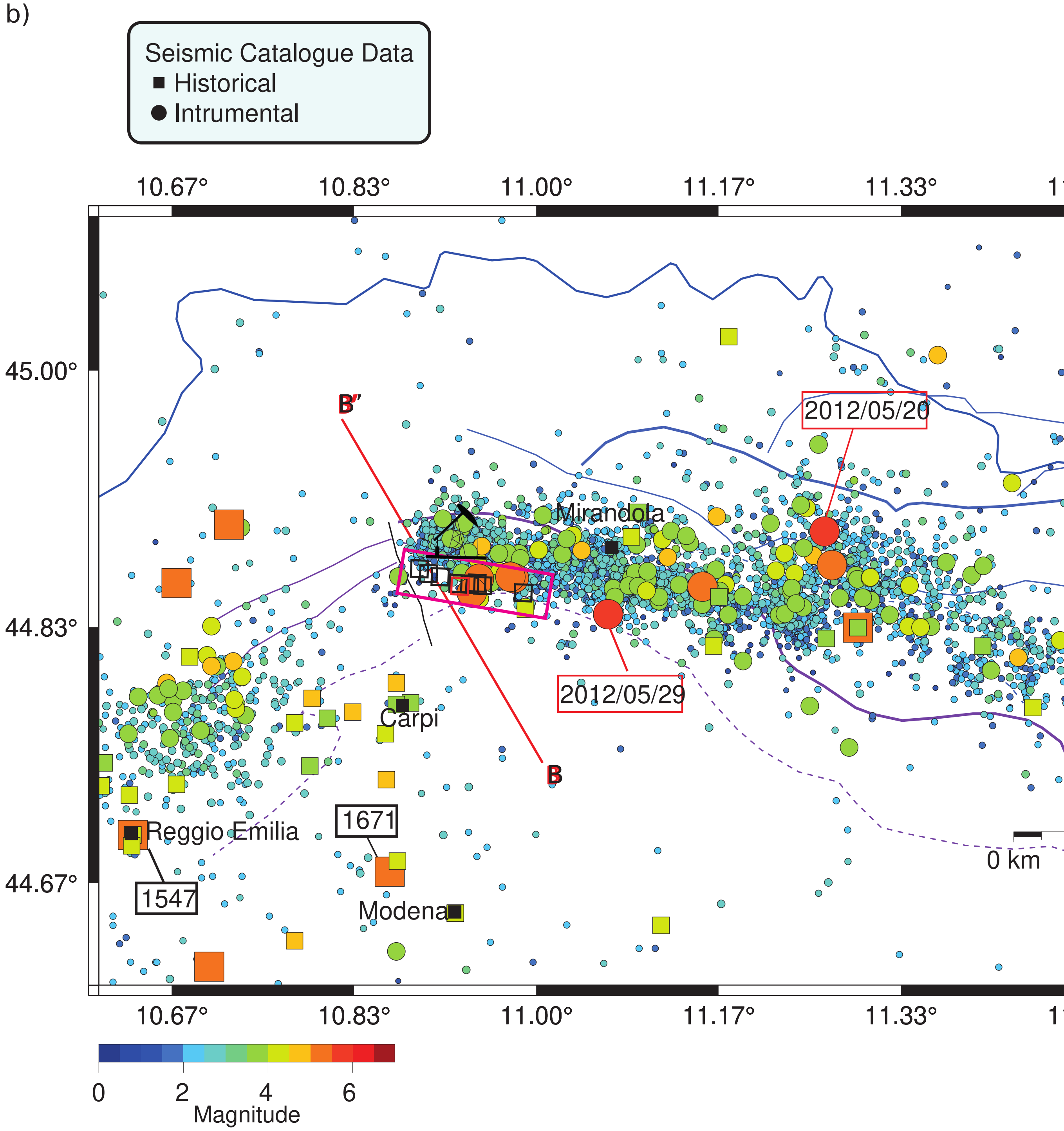

Seismic Catalogue Data
Historical
Intrumental
10.67°
10.83°
11.00°
11.17°
11.33°
45.00°
44.83°
44.67°
B'
B
Mirandola
2012/05/20
2012/05/29
Carpi
Reggio Emilia
1547
1671
Modena
0 km
0
2
4
6
Magnitude

c)

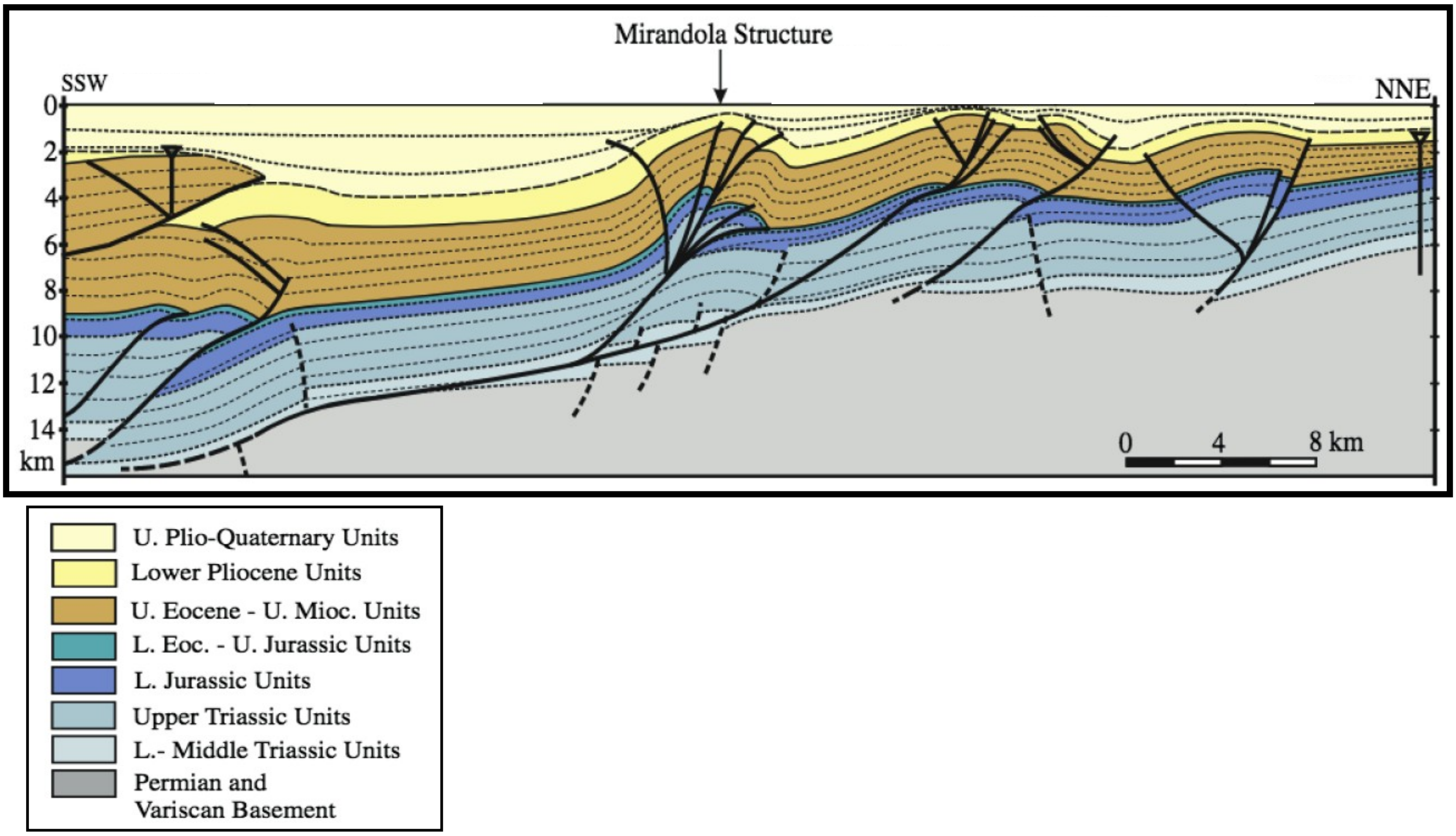
Mirandola Structure
SSW
NNE
0
2
4
6
8
10
12
14
km
0
4
8 km
U. Plio-Quaternary Units
Lower Pliocene Units
U. Eocene - U. Mioc. Units
L. Eoc. - U. Jurassic Units
L. Jurassic Units
Upper Triassic Units
L.- Middle Triassic Units
Permian and
Variscan Basement

Figure2

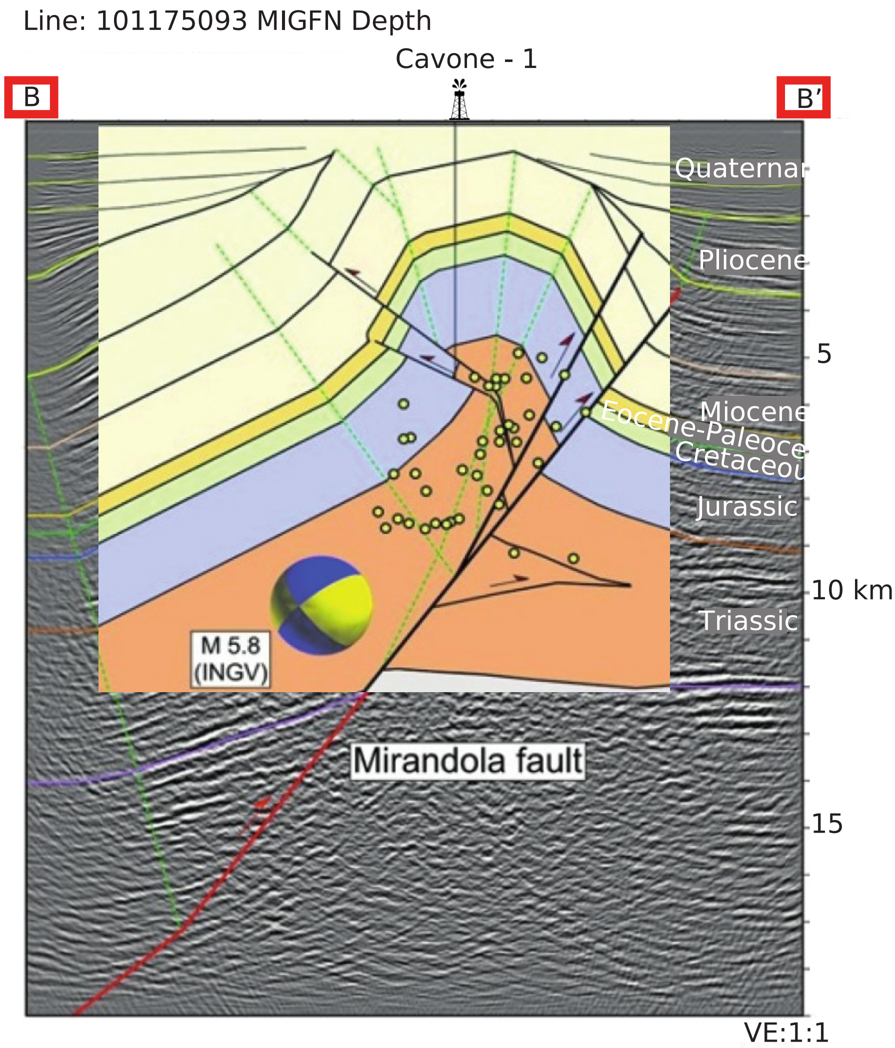

Line: 101175093 MIGFN Depth
Cavone - 1
B
B'
Quaternar
Pliocene
5
Miocene
Eocene-Paleoce
Cretaceou
Jurassic
10 km
Triassic
M 5.8
(INGV)
Mirandola fault
15
VE:1:1

Figure3

a)

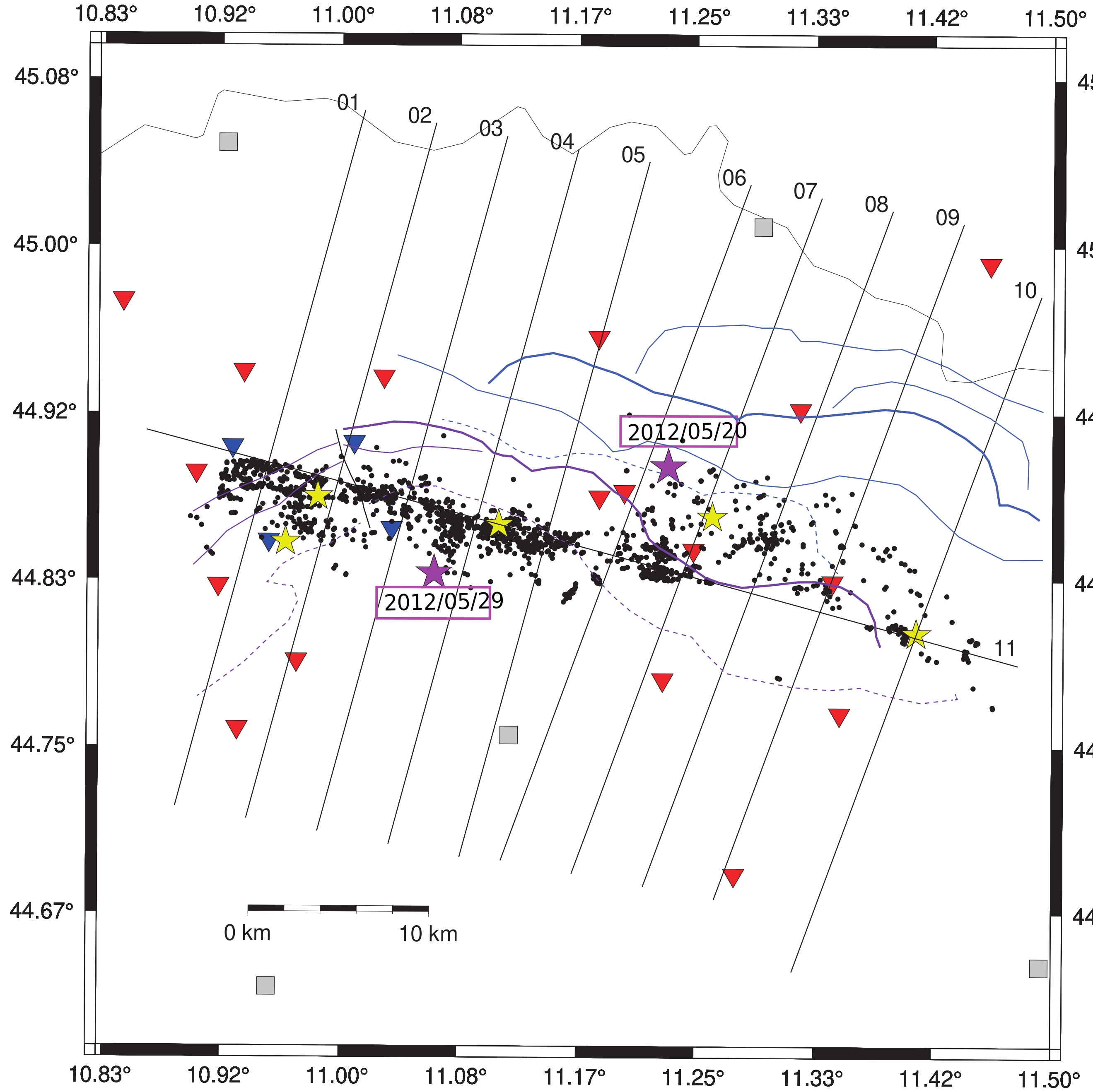

10.83°
10.92°
11.00°
11.08°
11.17°
11.25°
11.33°
11.42°
11.50°
45.08°
45.00°
44.92°
44.83°
44.75°
44.67°
01
02
03
04
05
06
07
08
09
10
11
2012/05/20
2012/05/29
0 km
10 km

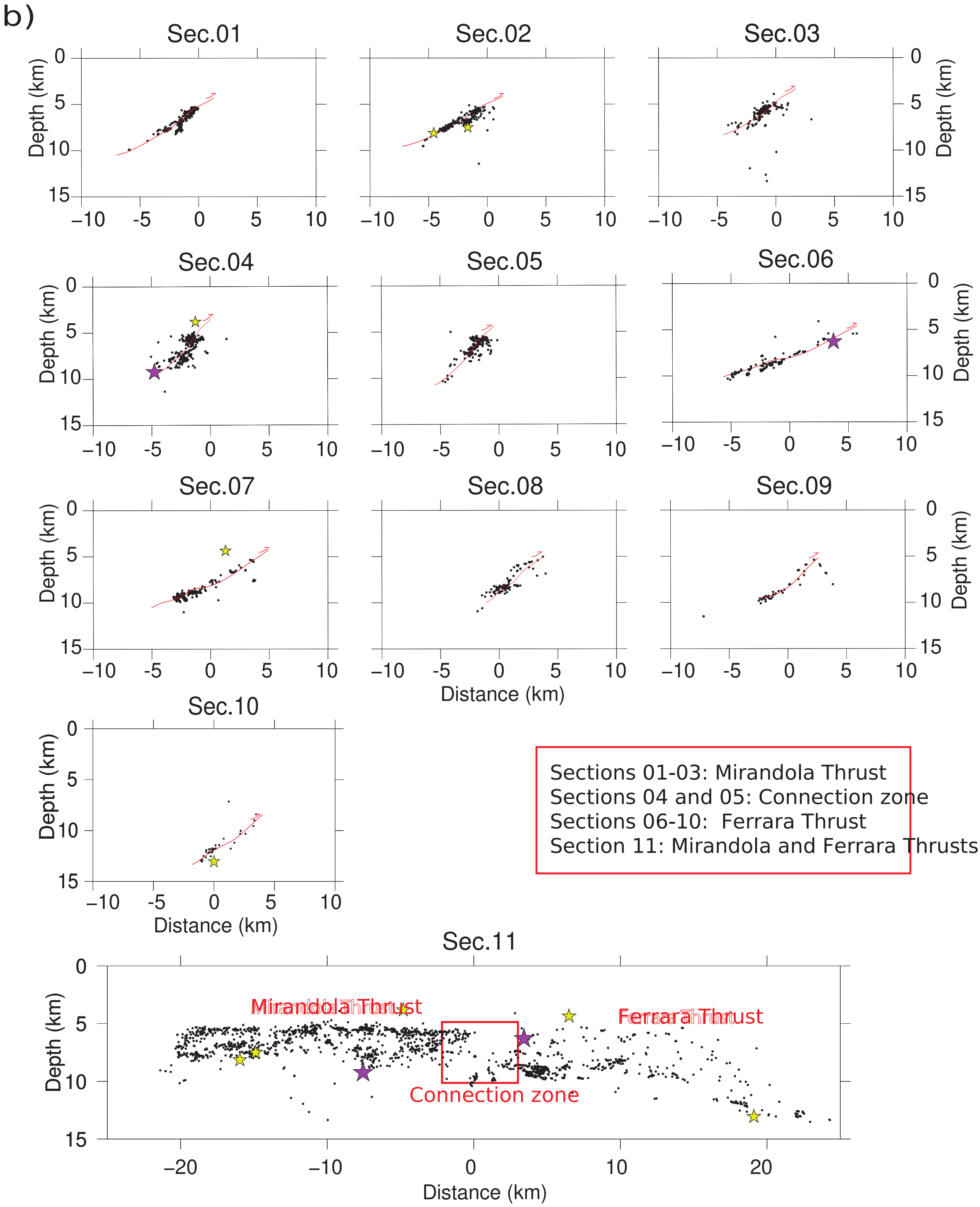
b)
Sec.01
Sec.02
Sec.03
Sec.04
Sec.05
Sec.06
Sec.07
Sec.08
Sec.09
Sec.10
Sec.11
Depth (km)
Distance (km)
Sections 01-03: Mirandola Thrust
Sections 04 and 05: Connection zone
Sections 06-10: Ferrara Thrust
Section 11: Mirandola and Ferrara Thrusts
Mirandola Thrust
Ferrara Thrust
Connection zone

Figure4

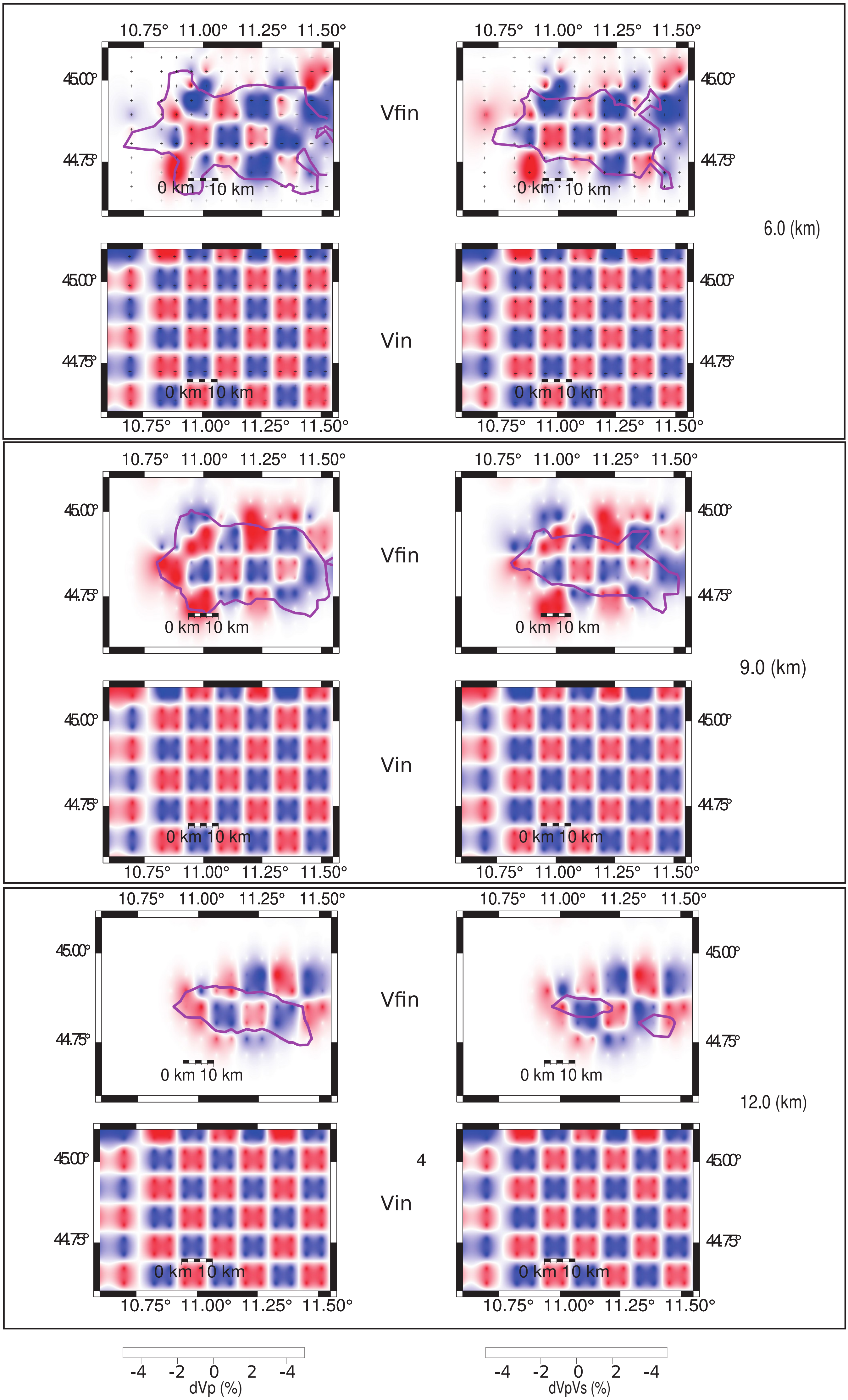
10.75° 11.00° 11.25° 11.50°
45.00°
44.75°
0 km 10 km
Vfin
Vin
6.0 (km)
9.0 (km)
12.0 (km)
4
-4 -2 0 2 -4
dVp (%)
-4 -2 0 2 -4
dVpVs (%)

Figure5

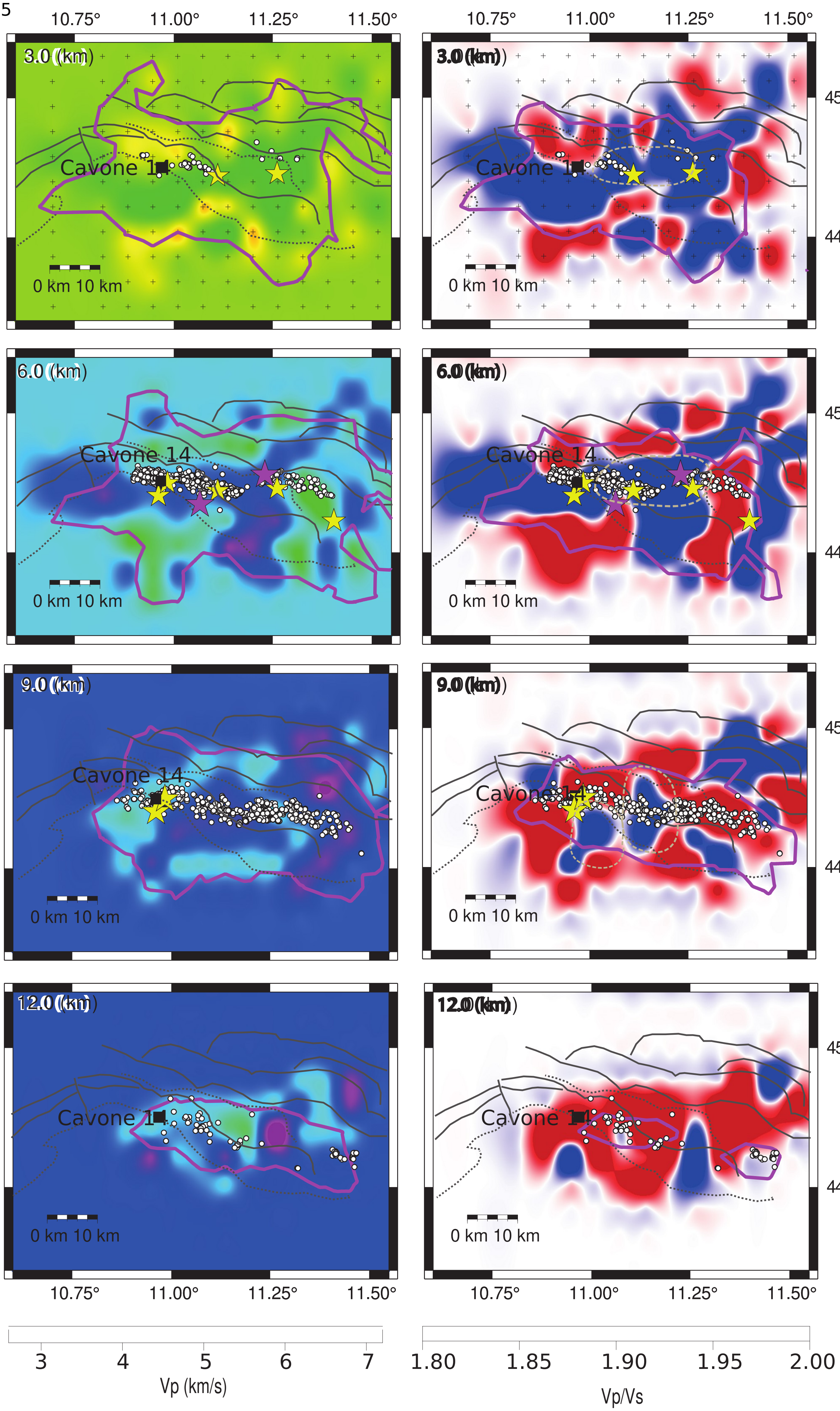

3.0 (km)
6.0 (km)
9.0 (km)
12.0 (km)
Cavone 14
0 km 10 km
10.75°
11.00°
11.25°
11.50°
45.00°
44.75°
3
4
5
6
7
Vp (km/s)
1.80
1.85
1.90
1.95
2.00
Vp/Vs

Figure6

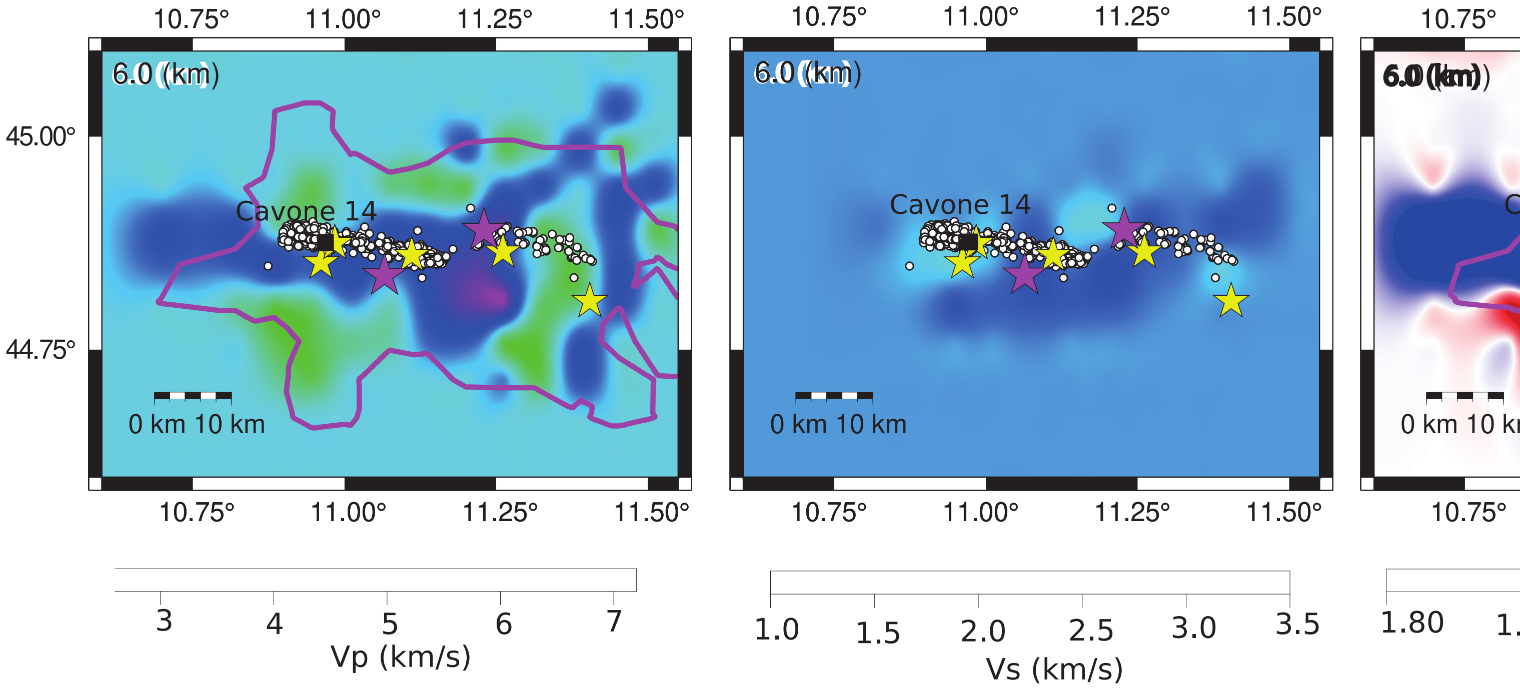

10.75°
11.00°
11.25°
11.50°
45.00°
44.75°
6.0 (km)
Cavone 14
0 km 10 km
3
4
5
6
7
Vp (km/s)
1.0
1.5
2.0
2.5
3.0
3.5
Vs (km/s)
1.80

Figure7

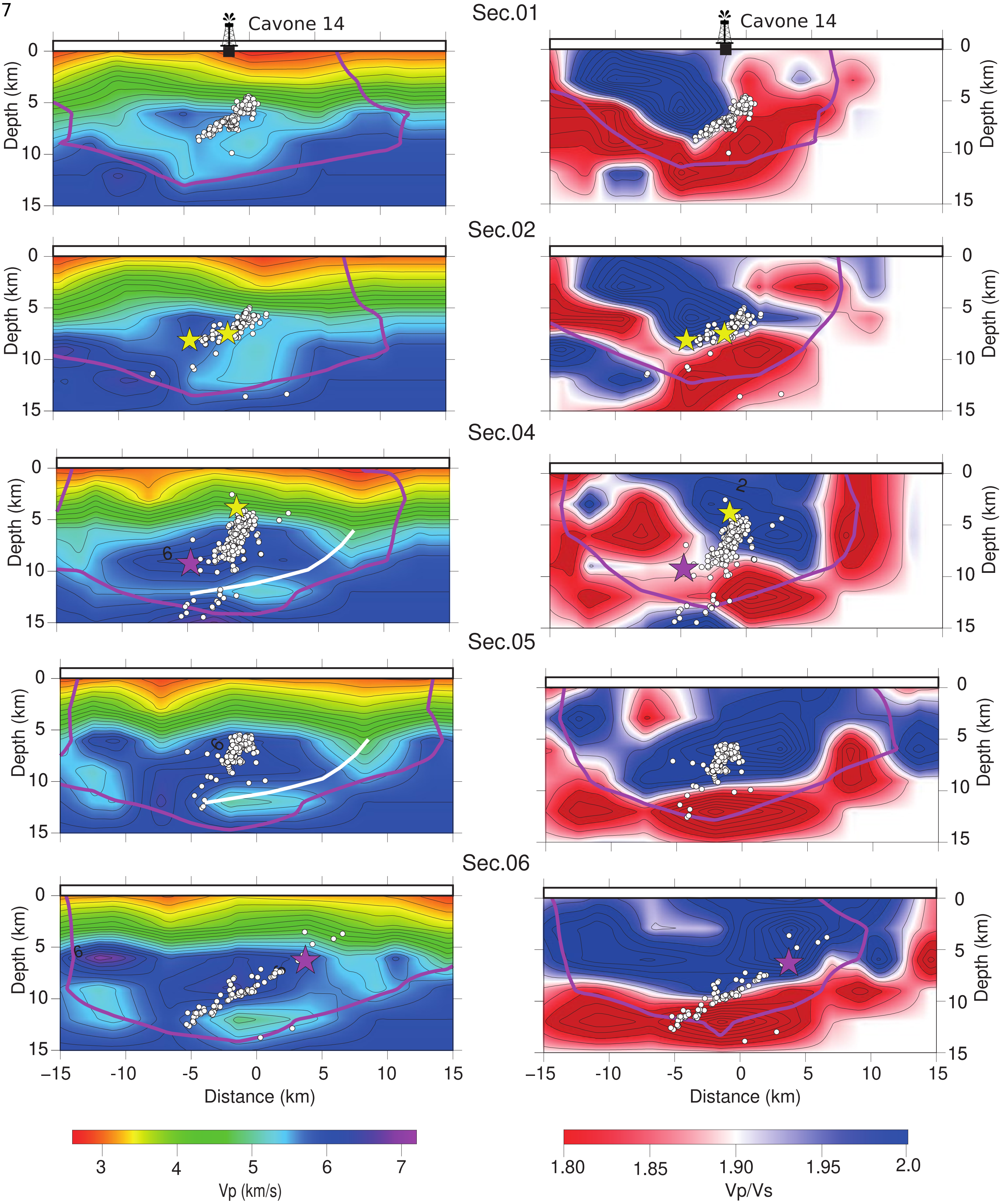

Cavone 14
Sec.01
Sec.02
Sec.04
Sec.05
Sec.06
Depth (km)
Distance (km)
Vp (km/s)
Vp/Vs

Figure8

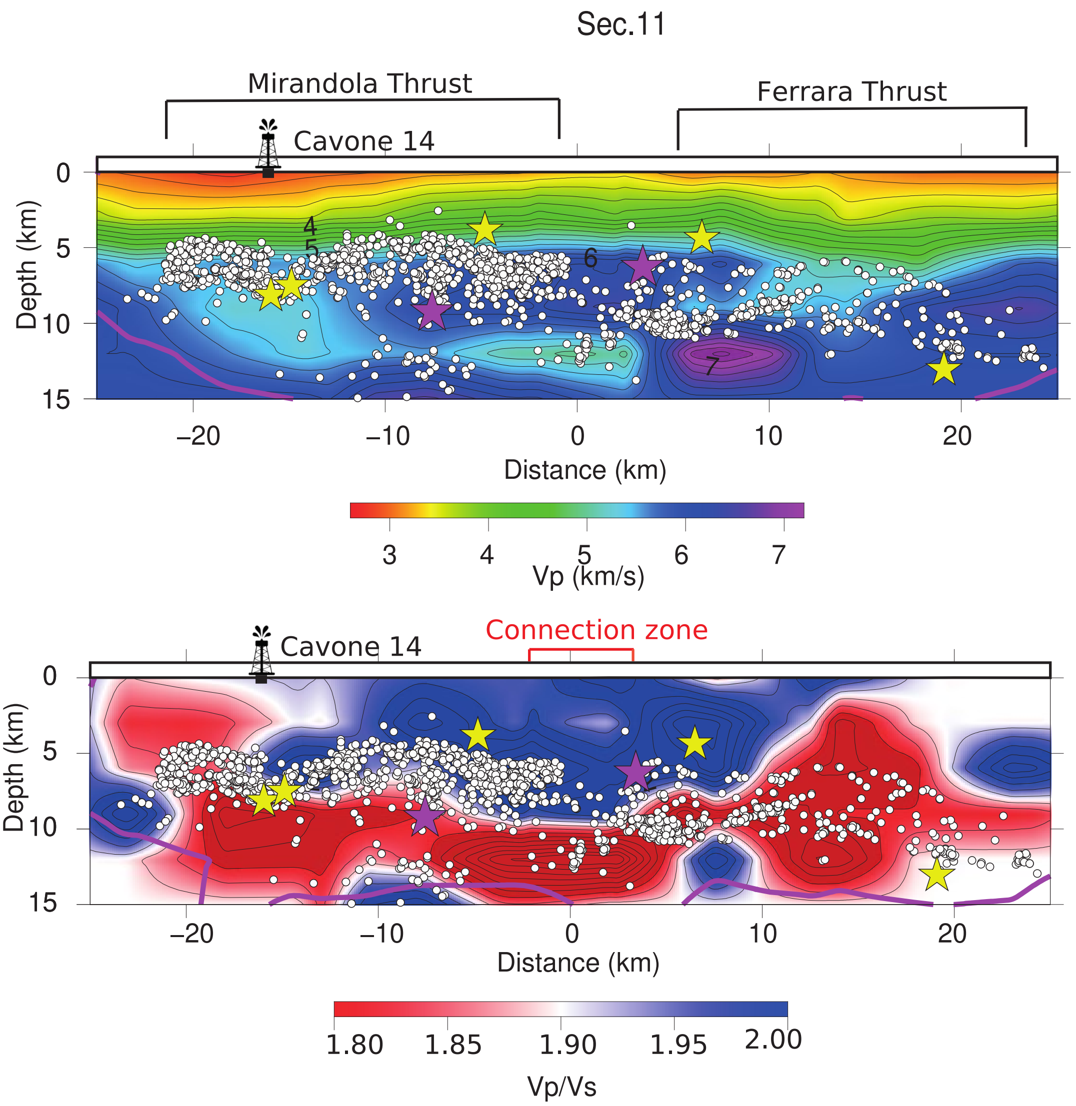
Sec.11
Mirandola Thrust
Ferrara Thrust
Cavone 14
Depth (km)
Distance (km)
Vp (km/s)
Connection zone
Cavone 14
Depth (km)
Distance (km)
Vp/Vs

Table1

Origin Time				Latitude			Longitude			Depth (km)	ML
Day	**Hour**	**Minute**	**Second**	**(°)**	**(')**	**('')**	**(°)**	**(')**	**('')**		
2012-05-20	**2**	**3**	**50.90**	**44**	**53.00**	**24.00**	**11**	**13.00**	**48.00**	**6.30**	**5.90**
2012-05-20	2	6	28.53	44	38.24	44.637	11	6.49	11.1082	13.9	4.94
2012-05-20	2	7	30.84	44	49.92	44.832	11	20.61	11.3435	3.39	4.9

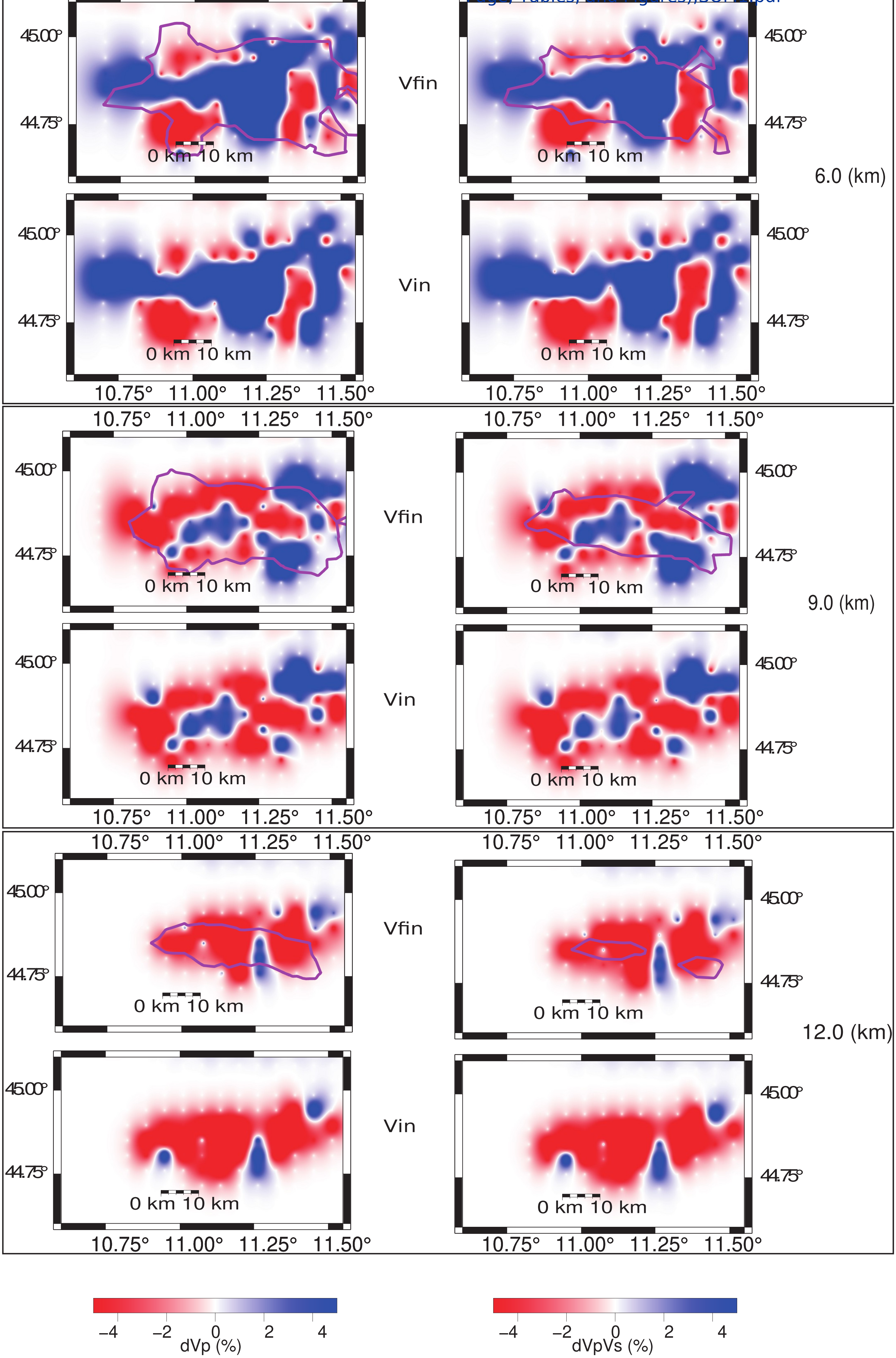
10.75° 11.00° 11.25° 11.50°
45.00°
44.75°
Vfin
Vin
6.0 (km)
9.0 (km)
12.0 (km)
0 km 10 km
−4 −2 0 2 4
dVp (%)
dVpVs (%)

SOM2

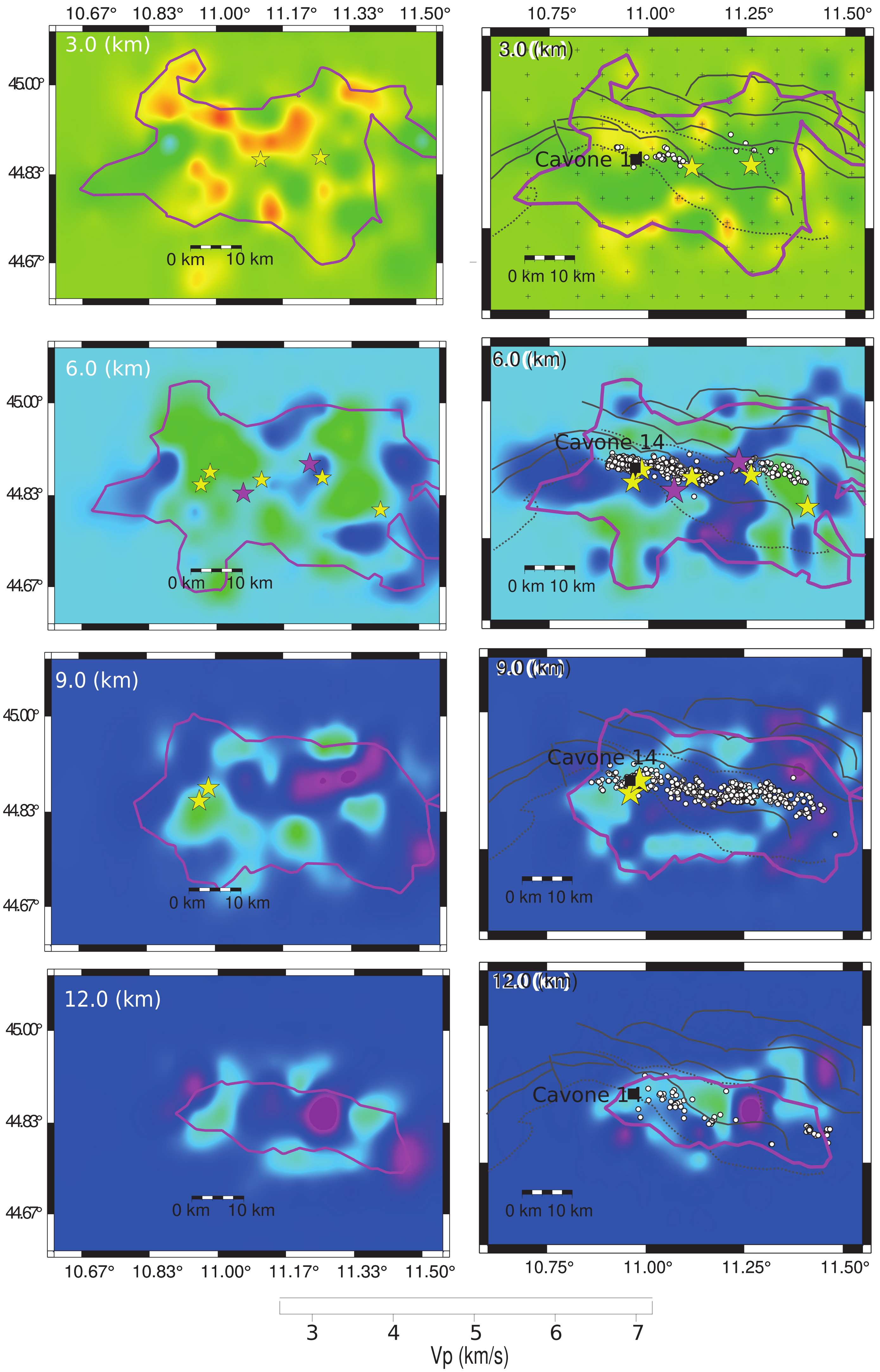

10.67°
10.83°
11.00°
11.17°
11.33°
11.50°
10.75°
11.00°
11.25°
11.50°
45.00°
44.83°
44.67°
3.0 (km)
6.0 (km)
9.0 (km)
12.0 (km)
Cavone 14
0 km 10 km
3
4
5
6
7
Vp (km/s)

SOM3

a)

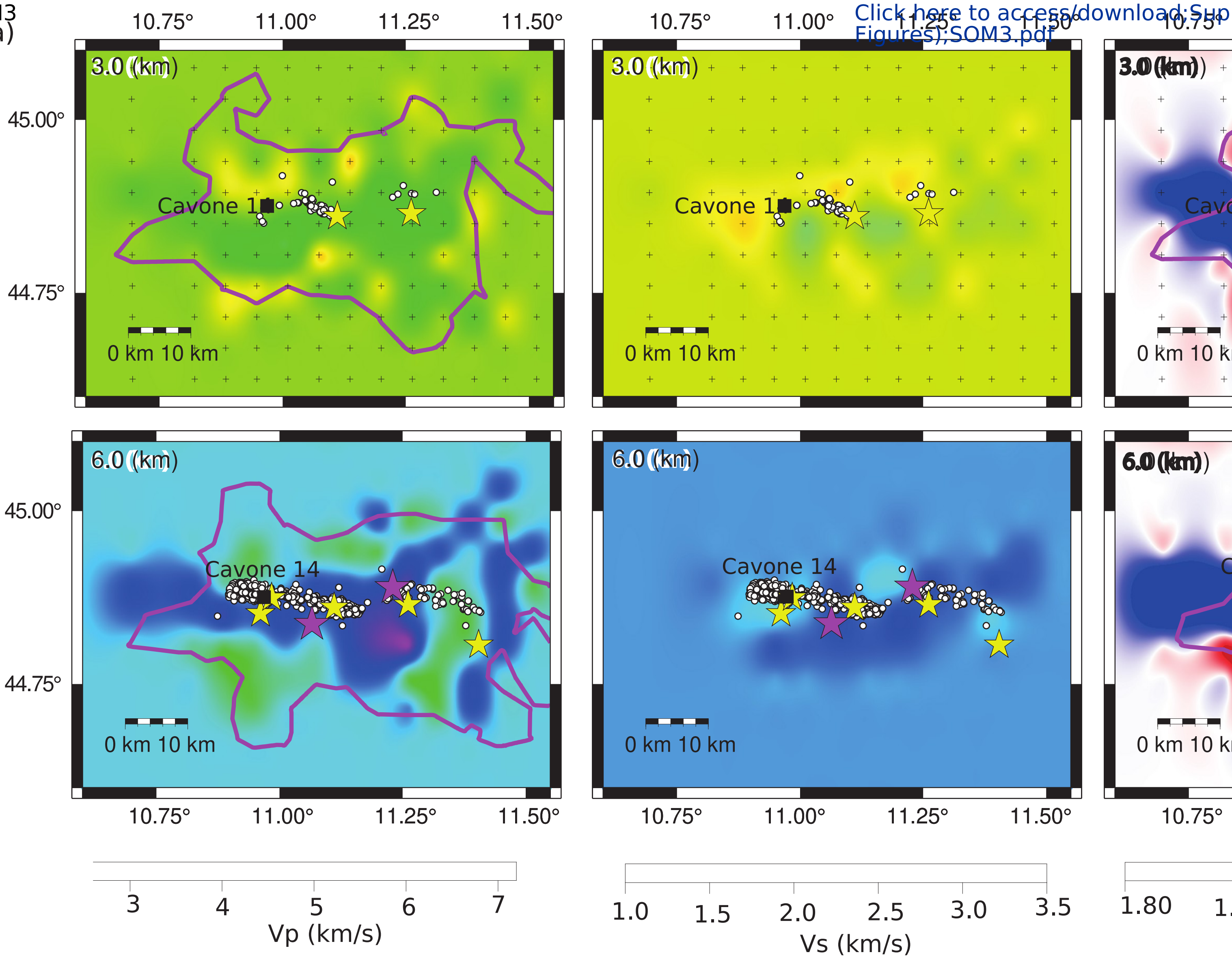
10.75°
11.00°
11.25°
11.50°
45.00°
44.75°
3.0 (km)
6.0 (km)
Cavone 1
Cavone 14
0 km 10 km
3
4
5
6
7
Vp (km/s)
1.0
1.5
2.0
2.5
3.0
3.5
Vs (km/s)
1.80

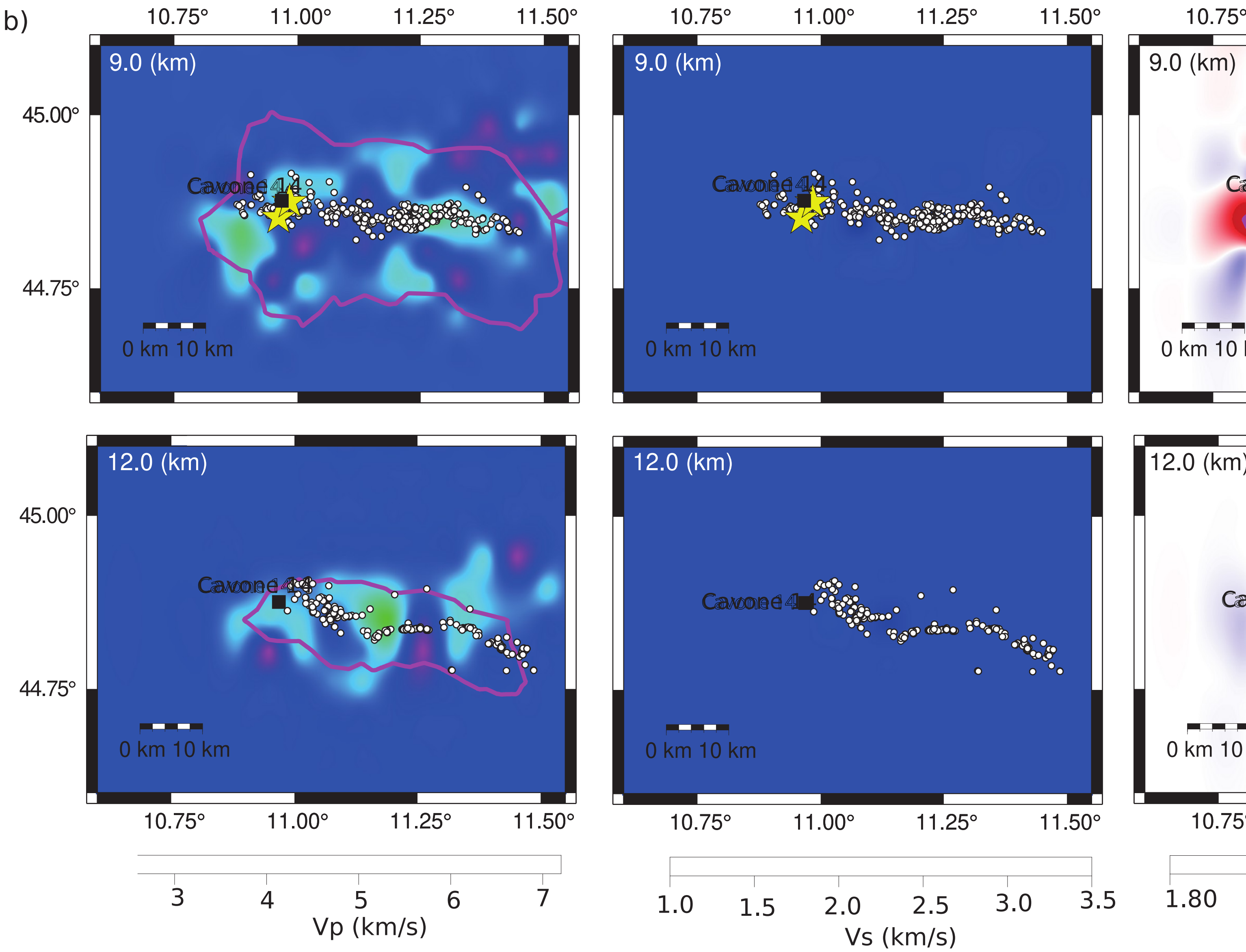

b)
10.75°
11.00°
11.25°
11.50°
45.00°
44.75°
9.0 (km)
12.0 (km)
Cavone 4.4
0 km 10 km
3
4
5
6
7
Vp (km/s)
1.0
1.5
2.0
2.5
3.0
3.5
Vs (km/s)
1.80

SOM4

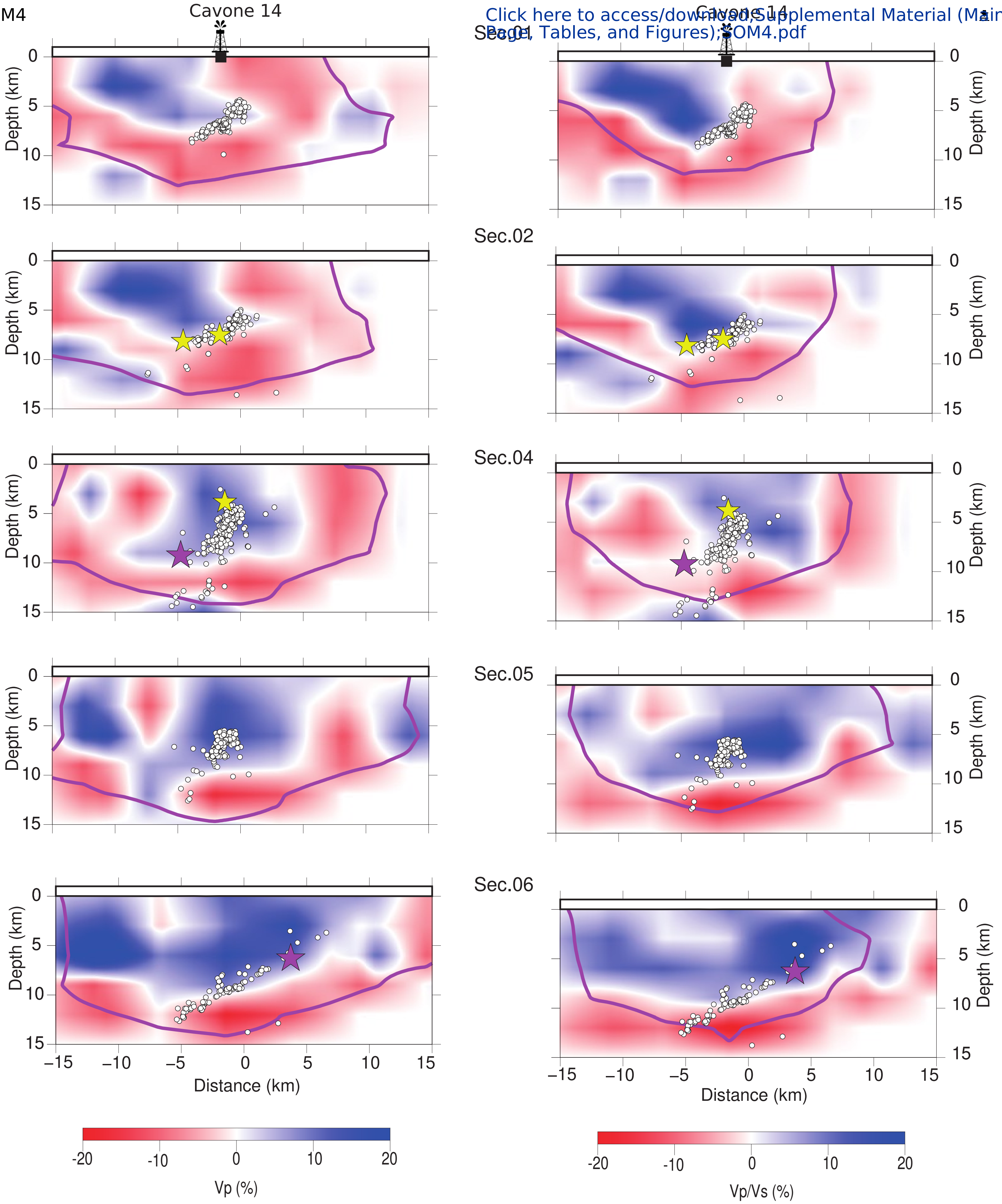
Cavone 14
Cavone 14
Sec.01
Sec.02
Sec.04
Sec.05
Sec.06
Depth (km)
Distance (km)
Vp (%)
Vp/Vs (%)

Supplemental Material of

Fault and fluid interaction during the 2012 Emilia (Northern Italy) seismic sequence

Fonzetti R., Valoroso L., De Gori P., Chiarabba C.

Supplemental Material for this article includes:

- STAB1: 1D starting velocity model from Chiarabba et al., 2014.
- SOM1: recovery test. The real dataset came from IS2 (absolute data modified, as described in paragraph 2, to obtain a V_p/V_s ratio which takes into account S-wave contribution);
- SOM2: comparison between the previous model and the new combined model obtained with IS1 and IS2;
- SOM3: The 3D V_p, V_s and V_p/V_s models obtained with IS2;
- SOM4: 3D V_p (from IS1) and V_p/V_s (from IS2) velocity anomalies of the cross sections, shown in Figure 6.

List of Supplemental Table Captions

STAB1: The 1D starting V_p velocity model used for TomoDD inversions.

List of Supplemental Figure Captions

SOM1: Recovery test at 6, 9 and 12 km depth (the dataset is the same as IS2). The pink line is the Spread Function (SF≤2). For each black box: above the final model obtained by inverting synthetic data; below, the synthetic model perturbed.

SOM2: Comparison between the previous model and the new combined model. The Vp and Vp/Vs models are close to each other. On the right, the previous model from Chiarabba et al., 2014; On the left, the new model obtained with the IS1 and IS2. The pink line is the Spread Function (SF≤2). The pink stars are the mainshocks *of 20th and 29th of May 2012 (the first from Govoni et al., 2014 and the second from TomoDD relocations). The yellow stars are the aftershocks with* $M_L \geq 4.0$. *The white dots represent aftershocks with* $M_L < 4$. *The aftershocks come from TomoDD relocations. The Cavone14 oil well is visible.*

SOM3: IS2 inversion. The pink line is the Spread Function ($SF \leq 2$). *For each layer (a) 3 and 6 km depth; b) 9 and 12 km depth), we show: the final 3D Vp, Vs and Vp/Vs model. The pink stars are the mainshocks of 20th and 29th May 2012 (the first from Govoni et al., 2014 and the second from TomoDD relocations). The yellow stars are the aftershocks with* $M_L \geq 4.0$. *The white dots represent aftershocks with* $M_L < 4$. *The aftershocks come from TomoDD relocations. Cavone14 oil well is visible.*

SOM4: Tomographic vertical sections of P-wave and V_p/V_s *models obtained with TomoDD inversion. The pink line is the Spread Function* ($SF \leq 2$). *Pink stars are the mainshocks of 20th and 29th May 2012 (the first from Govoni et al., 2014 and the second from TomoDD relocations). Yellow stars are the aftershocks with* $M_L \geq 4.0$. *White dots represent the aftershocks with* $M_L < 4.0$. *Aftershocks come from TomoDD relocations. The Cavone14 oil well is shown in section 1. Earthquakes occur +/- 2 km from the vertical sections.*

Layer (km)	Vp (km/s)
0	3.0
3	3.80
6	5.30
9	5.90
12	6.0
15	6.10
18	6.20
21	6.30
27	6.40

STAB1: The 1D starting V_p velocity model used for TomoDD inversions.

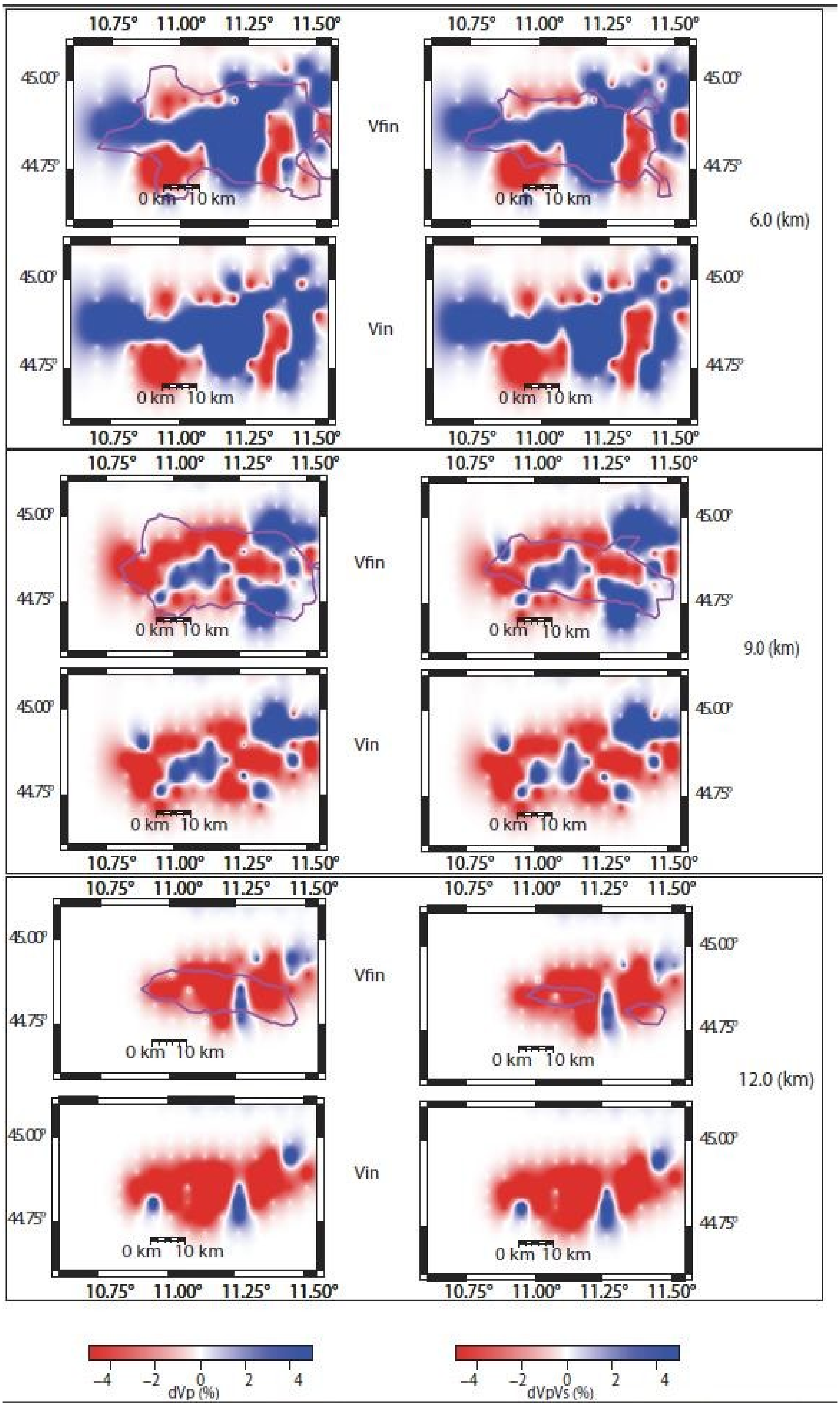

SOM1: Recovery test at 6, 9 and 12 km depth (the dataset is the same as IS2). The pink line is the Spread Function (SF≤2). For each black box: above the final model obtained by inverting synthetic data; below, the synthetic model perturbed.

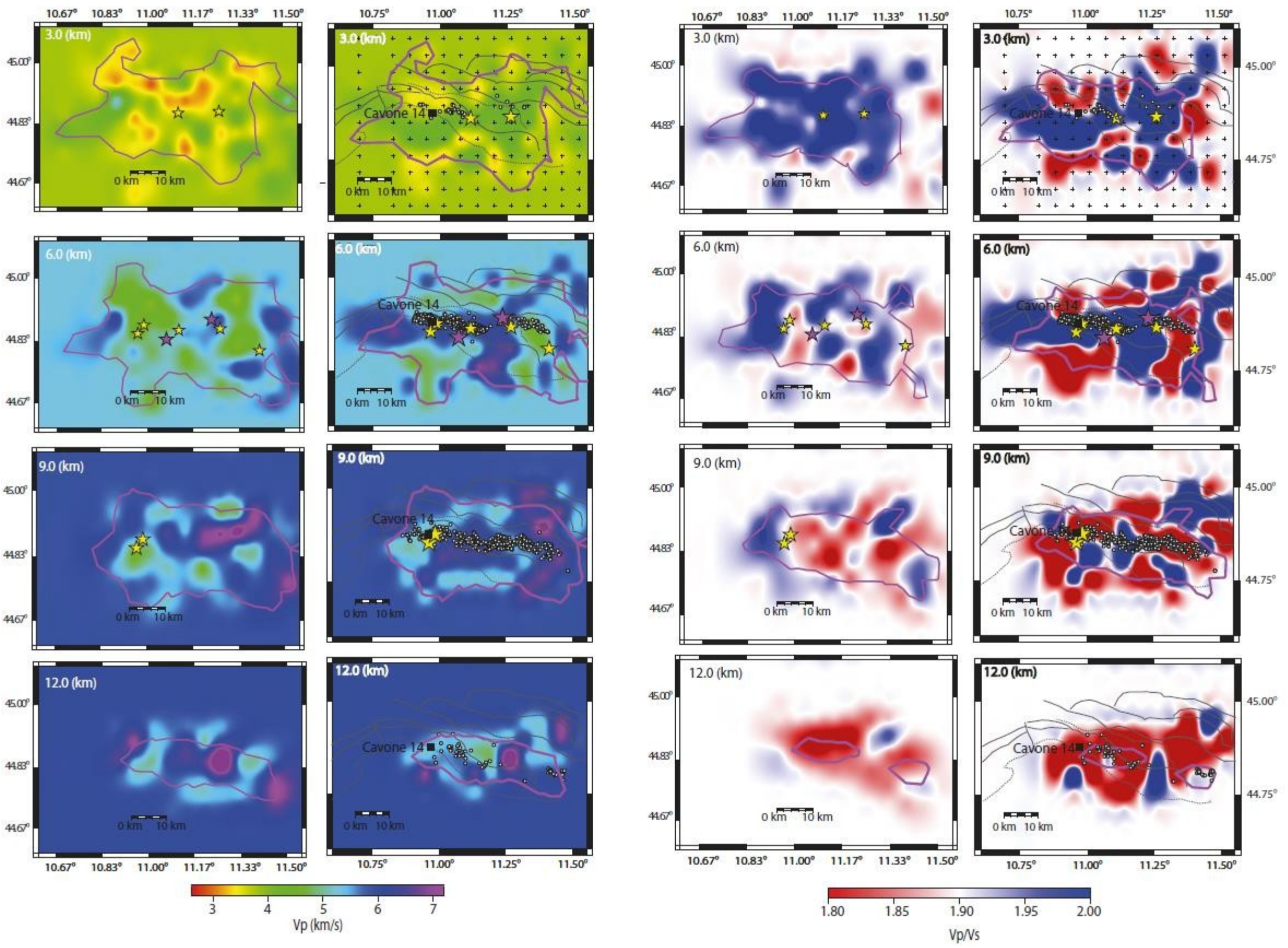

SOM2: Comparison between the previous model and the new combined model. The Vp and Vp/Vs models are close to each other. On the right, the previous model from Chiarabba et al., 2014; On the left, the new model obtained with the IS1 and IS2. The pink line is the Spread Function (SF ≤ 2). The pink stars are the mainshocks of 20th and 29th of May 2012 (the first from Govoni et al., 2014 and the second from TomoDD relocations). The yellow stars are the aftershocks with $M_L \geq 4.0$. The white dots represent aftershocks with $M_L < 4$. The aftershocks come from TomoDD relocations. The Cavone14 oil well is visible.

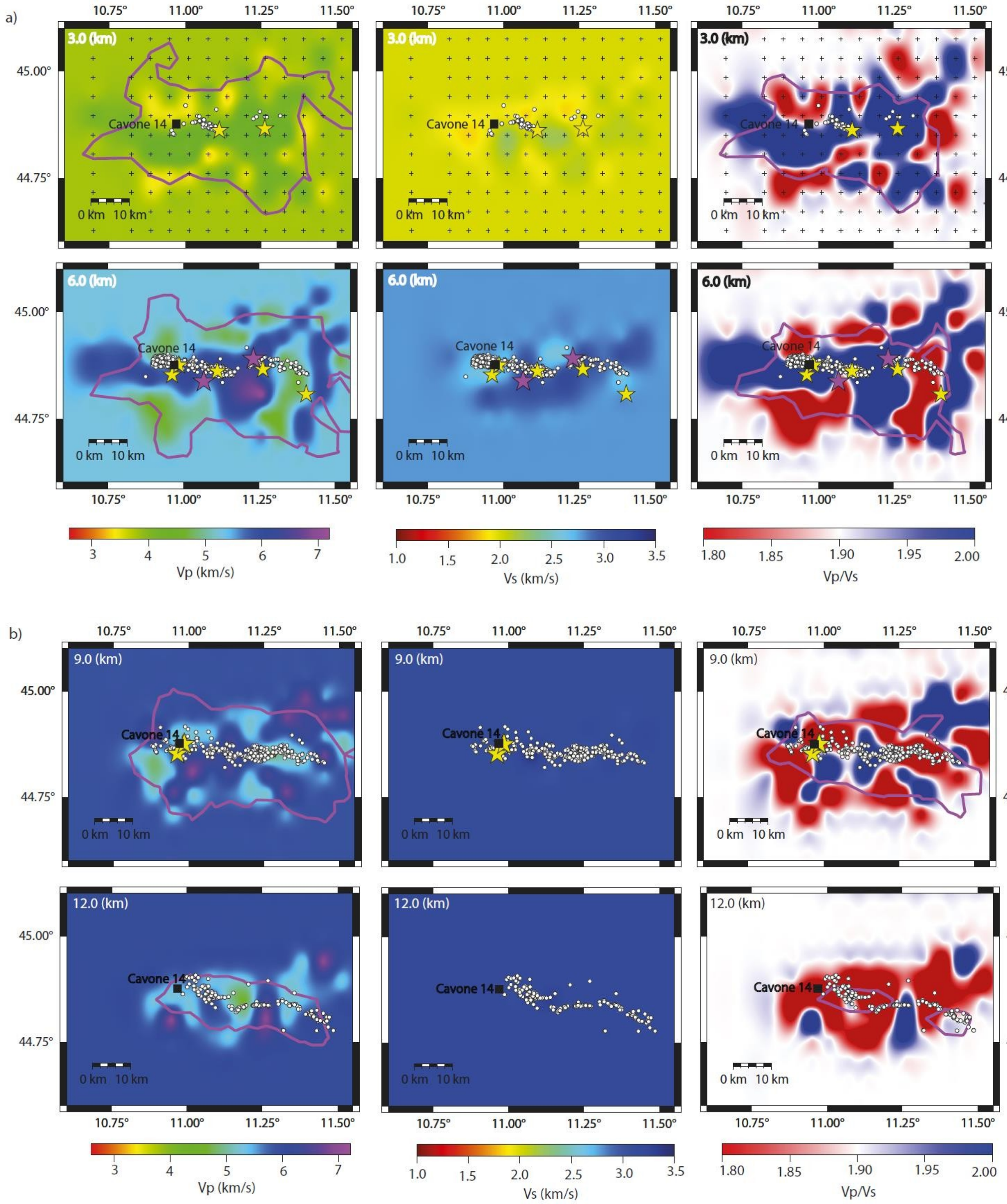

SOM3: IS2 inversion. The pink line is the Spread Function (SF≤ 2). For each layer (a) 3 and 6 km depth; b) 9 and 12 km depth), we show: the final 3D Vp, Vs and Vp/Vs model. The pink stars are the mainshocks of 20^{th} and 29^{th} May 2012 (the first from Govoni et al., 2014 and the second from TomoDD relocations). The yellow stars are the aftershocks with $M_L \geq 4.0$. The white dots represent aftershocks with $M_L < 4$. The aftershocks come from TomoDD relocations. Cavone14 oil well is visible.

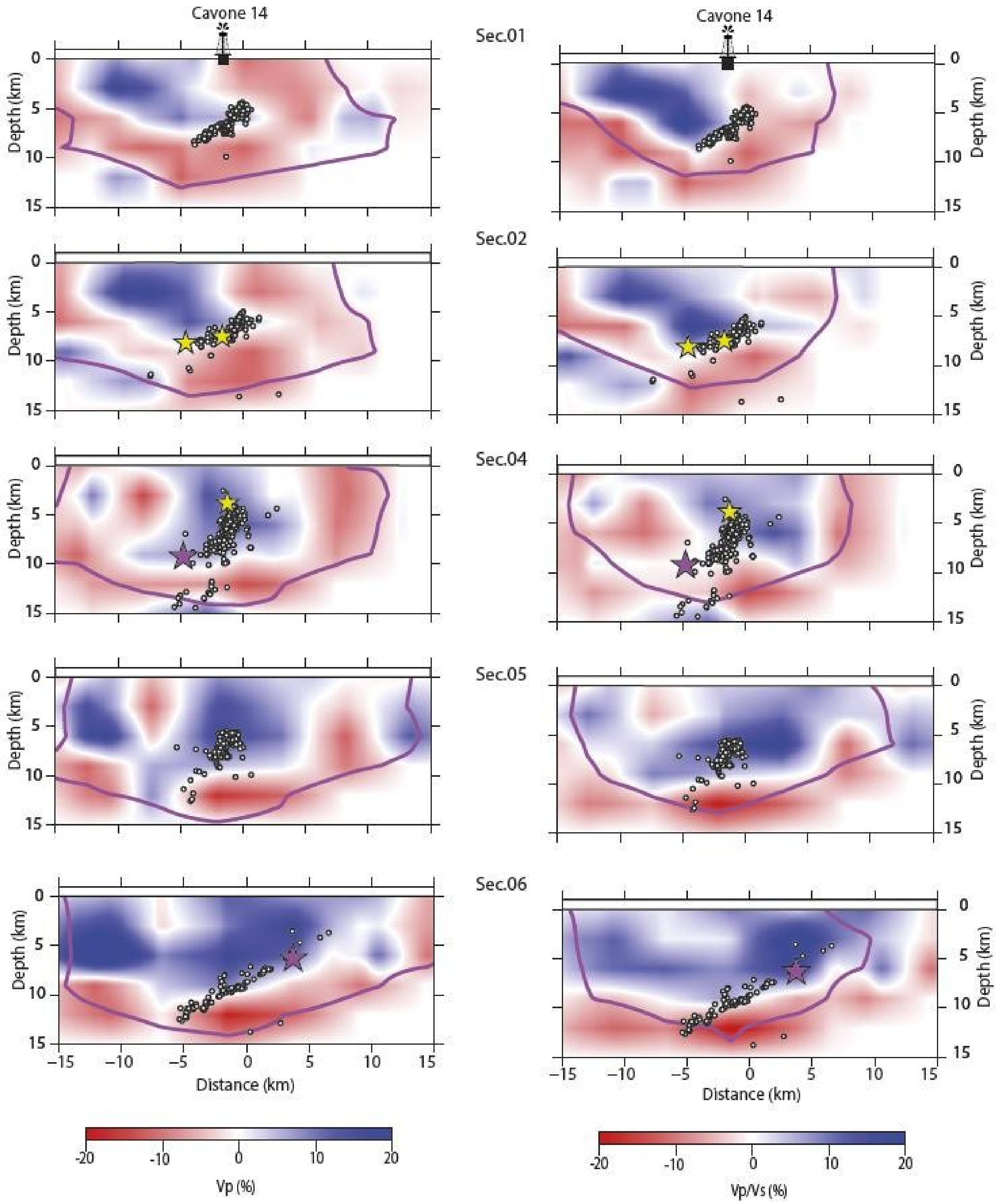

SOM4: Tomographic vertical sections of P-wave and V_P/V_S models obtained with TomoDD inversion. The pink line is the Spread Function (SF ≤ 2). Pink stars are the mainshocks of 20 th and 29th May 2012 (the first from Govoni et al., 2014 and the second from TomoDD relocations). Yellow stars are the aftershocks with $M_L \geq 4.0$. White dots represent the aftershocks with $M_L < 4.0$. Aftershocks come from TomoDD relocations. The Cavone14 oil well is shown in section 1. Earthquakes occur +/- 2 km from the vertical sections.

Layer (km)	**Vp (km/s)**
0	3.0
3	3.80
6	5.30
9	5.90
12	6.0
15	6.10
18	6.20
21	6.30
27	6.40